

© 2019 by Akshat Puri. All rights reserved.

MEASUREMENT OF ANGULAR AND MOMENTUM DISTRIBUTIONS OF CHARGED  
PARTICLES WITHIN AND AROUND JETS IN Pb+Pb AND  $pp$  COLLISIONS AT  
 $\sqrt{S_{NN}} = 5.02$  TeV WITH ATLAS AT THE LHC

BY

AKSHAT PURI

DISSERTATION

Submitted in partial fulfillment of the requirements  
for the degree of Doctor of Philosophy in Physics  
in the Graduate College of the  
University of Illinois at Urbana-Champaign, 2019

Urbana, Illinois

Doctoral Committee:

Professor Matthias Grosse Perdekamp, Chair  
Professor Anne Marie Sickles, Advisor  
<sup>1</sup> Professor Lance Cooper  
Professor Bryce Gadaway

# Abstract

2 Heavy ion collision experiments have been centered around studying the extreme state of matter formed in  
3 such collisions, the quark-gluon plasma. There have been efforts to measure and characterize this state of  
4 matter for almost two decades, first at the Relativistic Heavy Ion Collider and subsequently at the Large  
5 Hadron Collider. While there have been different approaches to study it, correlated particle showers called  
6 jets have found a special place as a probe of the QGP. Arising from highly energetic collisions between  
7 partons, jets are formed early enough in heavy ion collisions that they experience the formation of the QGP  
8 and its evolution. They are modified from what they would be in a vacuum, and studying these modifications  
9 can give insight into the properties of the QGP as well as the strong interaction.

10 Jet measurements can focus on a variety of observables like yields, momenta, or fragmentation patterns,  
11 each with its own limitations and advantages. This thesis presents a measurement of the angular distribution  
12 of charged particles around the jet axis as measured by the ATLAS detector for Pb+Pb and  $pp$  collisions  
13 with a center of mass energy of  $\sqrt{s_{NN}} = 5.02$  TeV. Comparing the measurement in the two systems shows  
14 that charged particles carrying a transverse momenta  $p_T$  of less than 4 GeV have a broader distribution  
15 in Pb+Pb collisions, while those with  $p_T > 4$  GeV have a narrower distribution. Furthermore, there is an  
16 enhancement for particles with  $p_T < 4$  GeV in Pb+Pb collisions, with the enhancement increasing up to 2  
17 for  $r < 0.3$  from the jet axis, and remaining constant for  $0.3 < r < 0.6$ . Charged particles with  $p_T > 4$  GeV  
18 show a small enhancement in the jet core for  $r < 0.05$ , and are increasingly suppressed up to 0.5 for  $r < 0.3$ .  
19 This depletion remains constant for  $0.3 < r < 0.6$ .

*For my Mother, Father, and Brother*

# Contents

|    |  |           |
|----|--|-----------|
| 23 | <b>Chapter 1 Introduction</b>            | <b>1</b>  |
| 24 | 1.1 Quantum Chromodynamics               | 1         |
| 25 | 1.2 Quark-Gluon Plasma                   | 4         |
| 26 | 1.3 Heavy Ion Collisions                 | 7         |
| 27 | 1.4 Jets and Jet Quenching               | 13        |
| 28 | 1.4.1 Jet Reconstruction                 | 16        |
| 29 | <b>Chapter 2 Major Jet Measurements</b>  | <b>19</b> |
| 30 | 2.1 Dijet Balance: $x_J$                 | 19        |
| 31 | 2.2 Modification of jet yields: $R_{AA}$ | 20        |
| 32 | 2.3 Jet Fragmentation                    | 23        |
| 33 | 2.4 Effective Quenching                  | 26        |
| 34 | 2.5 Jet Fluid model                      | 31        |
| 35 | 2.6 Hybrid Model                         | 34        |

# Chapter 1

## Introduction

36 This section shall discuss the theoretical background necessary to understand jet measurements. It will  
37 discuss the fundamentals of quantum chromodynamics (QCD), the heavy ion collision system and the quark  
38 gluon plasma that is formed, and finally jets and jet energy loss.  
39 remove Refs. [1] .

### 40 1.1 Quantum Chromodynamics

41 Quantum Chromodynamics is a gauge theory with SU(3) symmetry that describes the dynamics of the strong  
42 interactions between quarks and gluons. It is part of the Standard Model [2], the building blocks of which  
43 are shown in Figure 1.1.

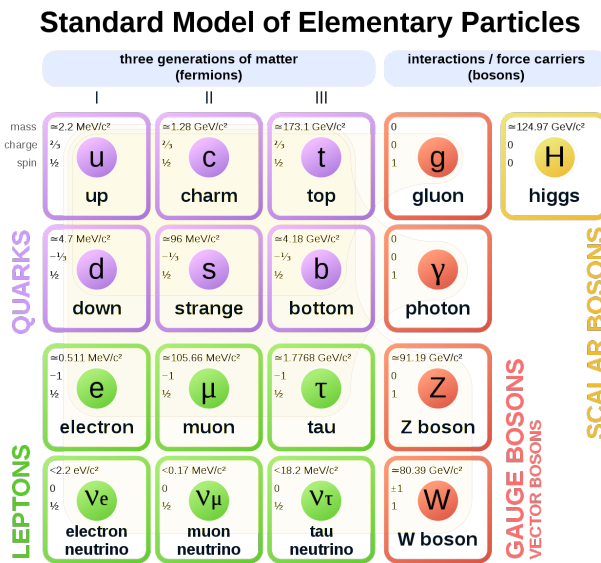


Figure 1.1: The elementary particles of the standard model. Figure taken from Ref. [3].

44 Quarks are fermions with a spin of  $1/2$ , and carry a fractional electric charge as well as a color charge.

45 They all have mass and come in six flavors: up, down, strange, charm, top, bottom. The lightest quarks  
 46 (u and d) combine and form stable particles, while the heavier quarks can only be produced in energetic  
 47 environments and decay rapidly. Gluons are gauge bosons (force carriers) with a spin of 1, and are what hold  
 48 quarks together. The dynamics of the quarks and gluons, collectively referred to as partons are described by  
 49 the QCD Lagrangian given as [4]:

$$\mathcal{L}_{\text{QCD}} = \sum_q \bar{\psi}_{q,a} (i\gamma^\mu \partial_\mu \delta_{ab} - g_s \gamma^\mu t_{ab}^C \mathcal{A}_\mu^C - m_q \delta_{ab}) \psi_{q,b} - \frac{1}{4} F_{\mu\nu}^A F^{A\mu\nu} \quad (1.1)$$

50 where  $\psi_{q,a}$  and  $\psi_{q,b}$  are quark-field spinors for a quarks with flavor  $q$ , mass  $m_q$ , and color  $a$  and  $b$  respectively,  
 51 with the values for  $a$  and  $b$  ranging from 1 to 3 (for the three colors). The  $\mathcal{A}_\mu^C$  corresponds to the gluon field  
 52 with  $C$  taking values from 1 through 8 (for the 8 types of gluons). The  $t_{ab}^C$  corresponds to the Gell-Mann  
 53 matrices that are the generators of the SU(3) group, and dictate the rotation of the quarks color in SU(3)  
 54 space when it interacts with a gluon. The coupling constant is encoded within  $g_s$ , which is defined by  
 55  $g_s \equiv \sqrt{4\pi\alpha_s}$ . The field tensor  $F_{\mu\nu}^A$  can be written in terms of the structure constants of the SU(3) group  
 56  $f_{ABC}$ , and is given by:

$$F_{\mu\nu}^A = \partial_\mu \mathcal{A}_\nu^A - \partial_\nu \mathcal{A}_\mu^A - g_s f_{ABC} \mathcal{A}^B \mathcal{A}^C \quad (1.2)$$

57 While many parallels can be drawn between Quantum Electrodynamics (QED, the theory that describes  
 58 photons and electrons) and QCD, the main difference between the two comes from the gluon-gluon interactions  
 59 allowed in QCD, making it non-Abelian. These interactions can be summarized as shown in Figure 1.2.

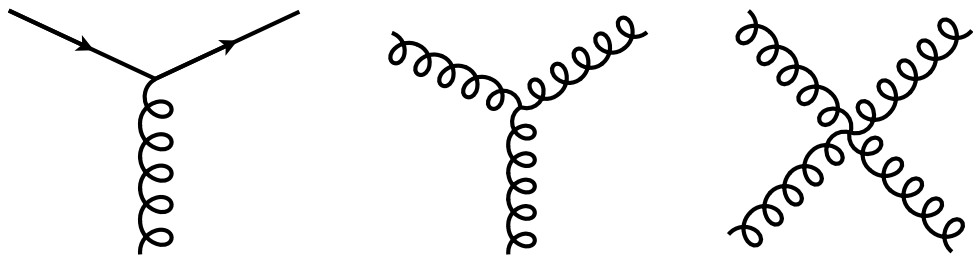


Figure 1.2: The allowed vertices in QCD. The vertices involving two or more gluons are unique to QCD and do not have a QED analog.

60 A core feature of QCD is that the coupling constant  $\alpha_s$  has an energy dependence shown in Figure 1.3.

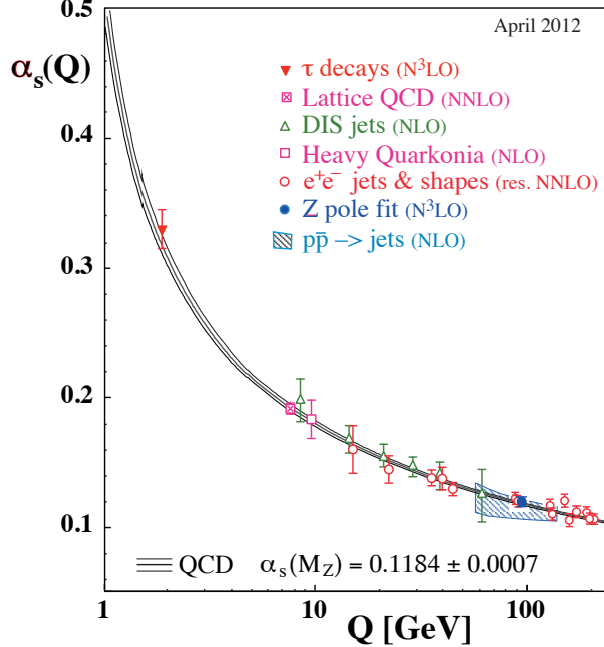


Figure 1.3: The running coupling constant  $\alpha_s$  as a function of the momentum transfer  $Q$ . Figure taken from Ref. [4].

61 This dependence can be expressed in terms of the  $\beta$  function as

$$Q^2 \frac{\partial \alpha_s(Q^2)}{\partial Q^2} = \beta(\alpha_s(Q^2)) \quad (1.3)$$

62 where  $Q$  is the momentum transfer in the particle reaction. The beta function can be expressed using  
63 perturbative QCD (pQCD) as

$$\beta(\alpha_s) = -(b_0 \alpha_s^2 + b_1 \alpha_s^3 + b_2 \alpha_s^4 \dots) \quad (1.4)$$

64 where the coefficients  $b_i$  depend on the number of colors and flavors. This running coupling constant is small  
65 and asymptotically tends to zero at large energy scales (or at small distances) and is large at small energy  
66 scales (large distances). This running coupling phenomenon leads to two key behaviors: asymptotic freedom  
67 and color confinement.

68     **Asymptotic Freedom:** At high energy scales (small distances), the QCD coupling constant  $\alpha_s$  is  
 69 small and tends to zero, implying a free particle behavior of quarks and gluons[5, 6]. This has been observed  
 70 by a variety of deep inelastic scattering (DIS) experiments [7–20]. These scattering experiments shown  
 71 in Figure 1.4, probe the interior of a nucleon using highly energetic leptons like electrons. First done by  
 72 MIT-SLAC [21, 22], these DIS experiments showed the weak  $Q^2$  dependence on the inelastic scattering  
 73 cross-sections , as well as Bjorken scaling [23], where the proton structure functions are independent of the  
 74 momentum transfer. These experiments revealed the point-like constituents of the proton and paved the  
 75 road to an asymptotically free theory.

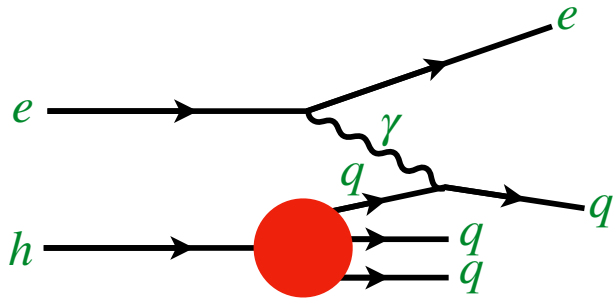


Figure 1.4: Schematic of the deep inelastic scattering experiment.

76     **Color Confinement** The opposite end of the running coupling constant phenomenon is color confinement.  
 77 Proved to be a consequence of asymptotic freedom in Ref [24], this property of QCD described in  
 78 Ref. [25] forbids the direct observation of free quarks and gluons, allowing only for composite particles that  
 79 are color singlets. While have been numerous efforts to understand the source of this phenomenon like in  
 80 Refs. [26–32], these are based on numerical calculations. An analytic proof of color confinement still escapes  
 81 description, and in fact, is one of the Millennium Problems [33].

## 82    1.2 Quark-Gluon Plasma

83 The quark-gluon plasma is a state of matter that comprises of free partons and is formed in extreme conditions  
 84 of temperature and pressure [34]. Its study is motivated by the fact that is the only way to access the  
 85 dynamics of partons that are otherwise confined within hadrons. Moreover, its thermodynamic properties are  
 86 of particular interest since it filled the early universe a few microseconds after the Big Bang [35]. The QGP  
 87 also forms the core of neutron-stars [36] and the recent detection of gravitational waves from a neutron-star  
 88 merger [37] has opened new avenues of investigation [38–40]. These studies have the potential to provide

89 information into the nuclear equation of state since the dynamics of the merger are sensitive to the behavior  
 90 of extremely dense nuclear matter [41]. The increase in temperatures and density during the merger results  
 91 in different pre- and post-merger signals of gravitational-waves that suggest a signature of a first-order  
 92 hadron-quark phase transition at extreme densities [42]. Colliders like RHIC and the LHC on the other  
 93 hand probe regions that have comparatively low baryon densities. Lattice QCD calculations in these regions  
 94 show that the transition between a hadronic gas and the QGP occurs at a temperature of approximately 160  
 95 MeV and corresponds to an energy density of  $0.5 \text{ GeV/fm}^3$  [43]. This is a smooth crossover that spans a  
 96 20–30 MeV temperature range, and can be seen in the QCD phase diagram shown in Figure 1.5. This phase  
 97 diagram shows the transition between free quarks and gluons within the QGP and the confined quarks and  
 gluons within hadrons, as a function of temperature  $T$  and baryon chemical potential  $\mu$ .

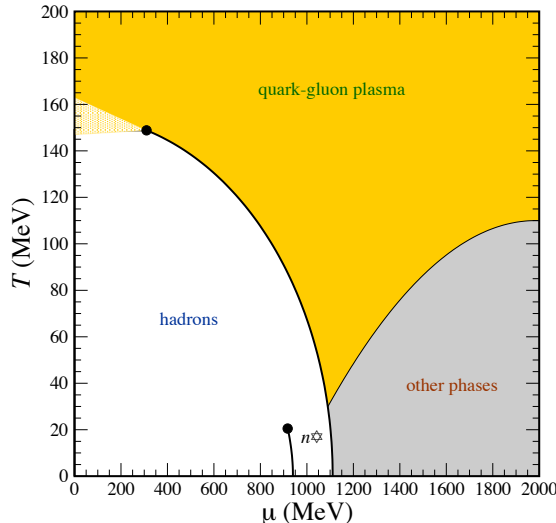


Figure 1.5: The QCD phase diagram of nuclear matter as a function of temperature  $T$  and baryon chemical potential  $\mu$ . The  $n\star$  denotes a neutron star. Figure from Ref. [44].

98  
 99 When formed in a heavy ion collision, this state of matter exists for 1–10 fm/c, depending on the collision  
 100 energy [45]. Thermal photons from the QGP reveal that it reaches temperatures of 300–600 MeV in central  
 101 collisions at 200 GeV [46] and 2.76 TeV [47], showing very little collision energy dependence. As the QGP  
 102 cools via expansion, its temperature drops below the critical temperature of QCD phase transitions and it  
 103 forms a hadron gas. This process, referred to as a chemical freeze-out, occurs at about 160 MeV [48–50]. The  
 104 hadrons formed in this stage continue to interact with each other, but have energies below the threshold for  
 105 inelastic particle production, resulting mainly in modifications to their momentum spectra. This continues  
 106 till the medium cools further and reaches what is called a thermal freeze-out at 100–150 MeV [51–54].

107 The QGP was initially thought to be a weakly coupled parton gas because of asymptotic freedom from

108 QCD [35]. The highly energetic collisions such as those at the LHC would imply a weak interaction between  
 109 the partons that make up the plasma. This would result in rare scatterings between the constituents of  
 110 the gas, washing out any spatial anisotropies based on “lumpy”-ness of the colliding nuclei or the collision  
 111 geometry. On the other hand, a strong coupling within the QGP would result in the pressure gradients in  
 112 the medium being driven by hydrodynamics and spatial anisotropies would be transformed to momentum  
 113 anisotropies in the particles produced as shown in Figure 1.6 [71]. In this picture, the non-uniform structure  
 114 of the colliding nuclei would cause a momentum anisotropy [55] that would be further enhanced when looking  
 115 at collisions that are less central and do not have perfect overlap between the colliding nuclei [56, 57]. These  
 116 observations were seen in azimuthal correlation measurements implying that the medium is indeed strongly  
 117 coupled [58–61].

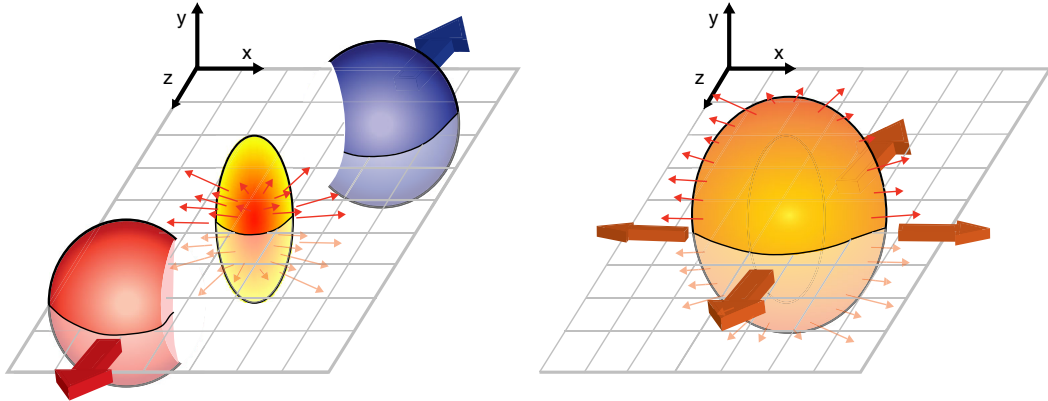


Figure 1.6: Schematic diagrams of the initial overlap region (left) and the final spatial anisotropy generated (right). Taken from [62].

118 A Fourier Transform of the angular distribution of charged hadrons in the collision debris can quantify  
 119 these momentum anisotropies and give the anisotropic flow coefficients  $v_n$ , defined as [63]:

$$\frac{d\bar{N}}{d\phi} = \frac{N}{2\pi} \left( 1 + 2 \sum_{n=1}^{\infty} v_n \cos(n(\phi - \Psi_n)) \right) \quad (1.5)$$

120 where  $\phi$  is the angle in the transverse plane,  $\Psi_n$  are the event plane angles, and  $N$  is the average number  
 121 of particles per event. Some of these coefficients are shown in Figure 1.7. The measured anisotropies can be  
 122 used to constrain the specific viscosity given by the ratio of viscosity to entropy density,  $\eta/s$ , and have shown  
 123 that the QGP has a  $\eta/s$  of near the theoretical minimum of  $1/4\pi$  [64].

124 The Bjorken energy density of the QGP can be derived using [67]:

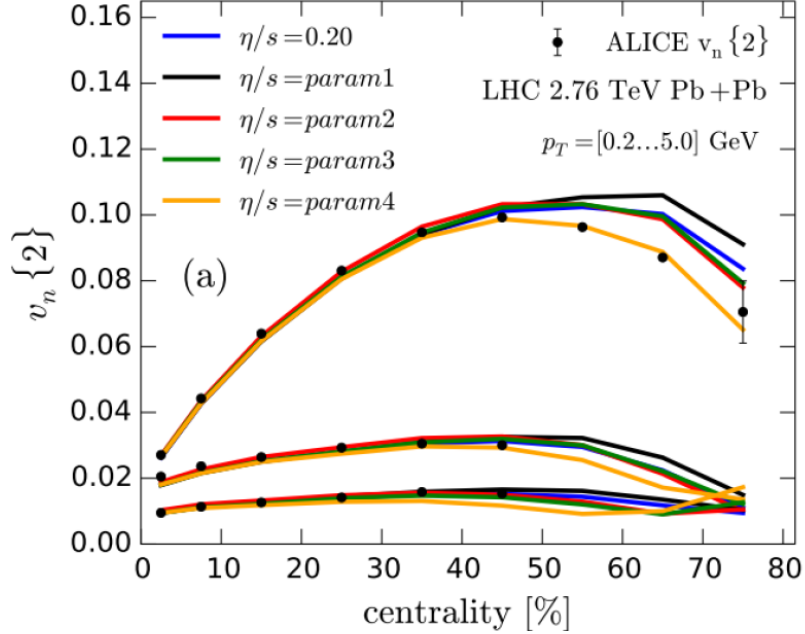


Figure 1.7: Comparison of a hydrodynamic model from [65] to anisotropy measurements by ALICE [66] for different parameterizations of  $\eta/s$  and for different  $v_n$ ,  $n = 2, 3, 4$  from top to bottom, as a function of collision centrality.

$$\varepsilon \geq \frac{dE_{\text{T}}/d\eta}{\tau_0 \pi R^2} = \frac{3}{2} \langle E_{\text{T}}/N \rangle \frac{dN_{\text{ch}}/d\eta}{\tau_0 \pi R^2} \quad (1.6)$$

where  $dN_{\text{ch}}/d\eta$  is the number of charged particles produced per unity pseudorapidity,  $dE_{\text{T}}/d\eta$  is the transverse energy per unit pseudorapidity,  $\tau_0$  is the thermalization time,  $R$  is the nuclear radius, and  $E_{\text{T}}/N \approx 1$  GeV is the transverse energy per emitted particle. As shown in Figure 1.8, the energy density at the LHC was measured to be approximately  $15 \text{ GeV/fm}^3$ , much higher than the values measured at RHIC [68, 69].

### 1.3 Heavy Ion Collisions

Heavy ion collisions can be used as a tool to study the quark-gluon plasma (QGP) [34]. This section shall focus on the

In a heavy ion collision, the colliding nuclei are accelerated to relativistic energies and are Lorentz contracted discs. In the case of a Pb+Pb collision the relativistic  $\gamma$  factor is between 100 and 2500 for beam rapidities of  $y = 5.3$  and  $8.5$ . Each nucleus contains many colored quarks and antiquarks, with three more quarks than anti-quarks per nucleon, with the  $q\bar{q}$  popping in and out of the vacuum due to quantum

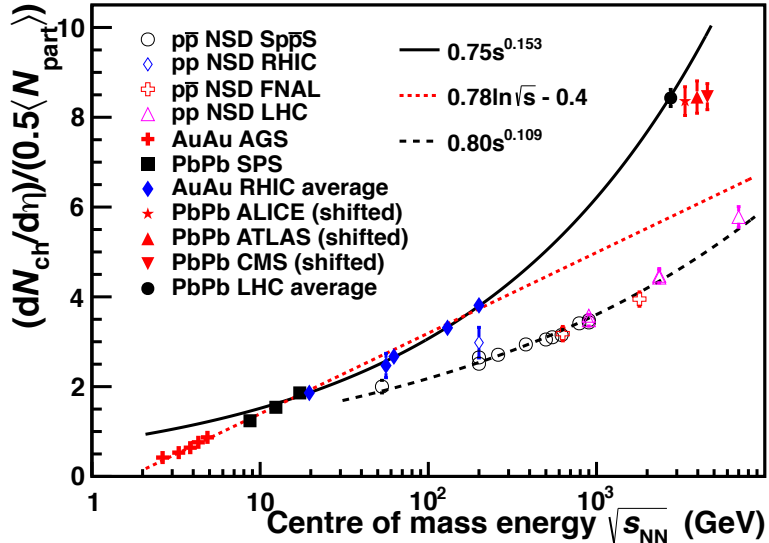


Figure 1.8:  $dN_{\text{ch}}/d\eta$  per colliding nucleon pair as a function of collision energy in  $pp$  and nucleus-nucleus collisions [70].

fluctuations. These  $q\bar{q}$  pairs are sources of transverse color fields and the corresponding force carriers, the gluons.

When these pancake like discs collide, their color fields interact and there is a color charge exchange, producing longitudinal color fields that fill the space between the receding discs. While the maximum energy density in the process occurs just at the collision, the energy density 1 fm/c after the collision is 12 GeV/fm<sup>3</sup>, much higher than the 500 MeV/fm<sup>3</sup> in a typical hadron. Lattice QCD calculations in thermodynamics show that at these energies, the partons produced in the collision cannot be treated as a collection of distinct hadrons.

After the collision the energy density between the receding nuclei starts to decrease as the QGP cools and expands. This process, seen in Figure 1.9, continues till the energy density drops to below that within a hadron and the fluid “hadronizes”. These individual hadrons briefly scatter off of each other before they freely fly towards the detector (freeze-out).

While Figure 1.9 shows snapshots of a head on (central) collision between two large nuclei, it is possible to have collisions where the impact parameter is larger and hence the overlap region is smaller. These collisions, called peripheral collisions, qualitatively undergo the same process described above, with the size and shape of the QGP being different.

The basic parameters of a heavy ion collision such as the number of participants  $N_{\text{part}}$  and number of binary collisions  $N_{\text{coll}}$  can be determined using the Glauber Monte Carlo simulations [72, 73]. This technique

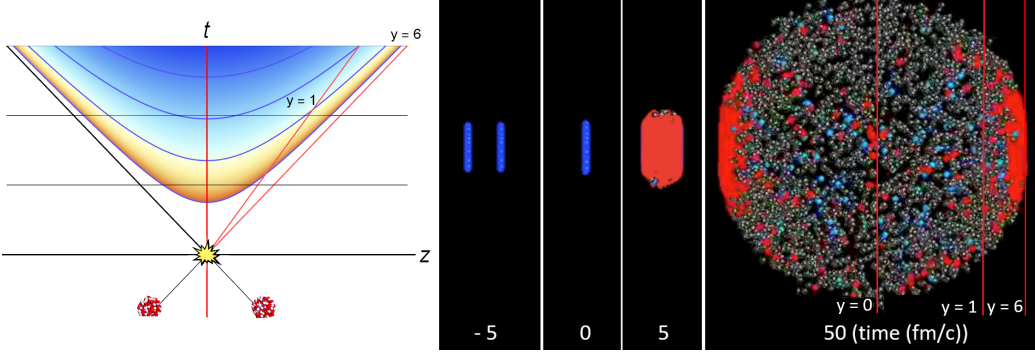


Figure 1.9: (left) Space-time diagram for a heavy ion collision. The color is indicative of the temperature of the QGP formed. (right) Snapshots of a heavy ion collision at  $\sqrt{s_{NN}} = 2.76$  TeV at different times. The Lorentz contracted nuclei are in blue while the QGP is in red. Figure from Reference [71].

154 considers a nucleus-nucleus collision as a collection of independent binary nucleon-nucleon collisions; the  
 155 colliding nuclei are modeled as a set of uncorrelated nucleons being positioned within the nucleus based on a  
 156 the nuclear density function uniform in azimuthal and in polar angles. The nuclear density function shown in  
 157 Figure 1.10 for Au and Cu, is given by:

$$\rho(r) = \rho_0 \frac{1 + w(r/R)^2}{1 + e^{\frac{r-R}{a}}} \quad (1.7)$$

158 where  $\rho_0$  is the nucleon density,  $R$  is the nuclear radius,  $a$  is the skin depth,  $w$  corresponds to deviations  
 159 from a circular shape and is typically zero for larger nuclei like Cu, W, Au, Pb, and U. For the Pb nuclei  
 160 used at the LHC,  $w = 0$ ,  $R = 6.62$  fm and  $a = 0.55$  fm [74].

161 They are then arranged with a random impact parameter  $b$  based on the distribution  $d\sigma/db = 2\pi b$  and  
 162 projected onto the  $x - y$  plane as shown in Figure 1.11. They are then made to travel on straight trajectories,  
 163 colliding if  $d \leq \sqrt{\sigma_{\text{inel}}^{\text{NN}}/\pi}$ , where  $d$  is the distance between the nucleons in a plane transverse to the beam  
 164 axis and  $\sigma_{\text{inel}}^{\text{NN}}$  is the inelastic scattering cross section. [75, 76]

165 An important parameter for colliding nuclei A and B with  $A$  and  $B$  nucleons is the thickness function  
 166  $T_{AB}$ . It describes the effective overlap area in which specific nucleons in the two colliding nuclei can interact.  
 167 It can be defined in terms of the probability per unit area of a given nucleon being located at a particular  
 168 distance  $s$  within the nucleus. For the colliding nuclei A and B, this is given by  $T_A(\mathbf{s}) = \int \rho_A(\mathbf{s}, z_A) dz_A$  and  
 169  $T_B(\mathbf{s}) = \int \rho_B(\mathbf{s}, z_B) dz_B$ . Then,  $T_{AB}$  is given by

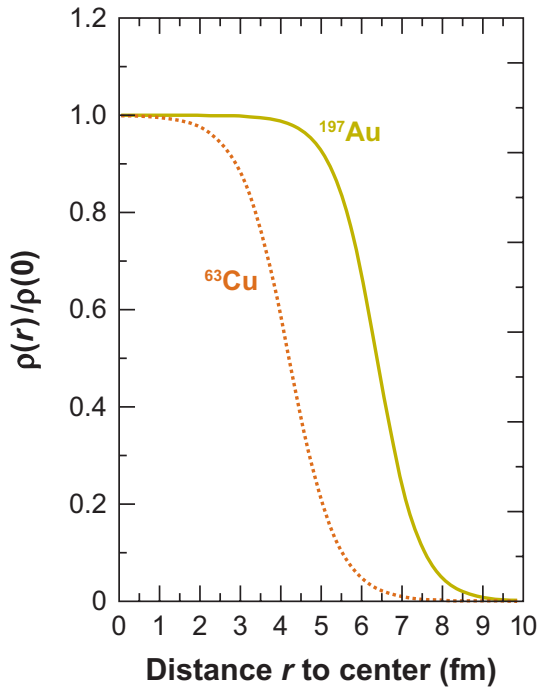


Figure 1.10: The nuclear density distributions for nuclei used at RHIC: Cu ( $w = 0$ ,  $R = 4.2$  fm and  $a = 0.48$  fm) and Au ( $w = 0$ ,  $R = 6.38$  fm and  $a = 0.535$  fm) [74, 75].

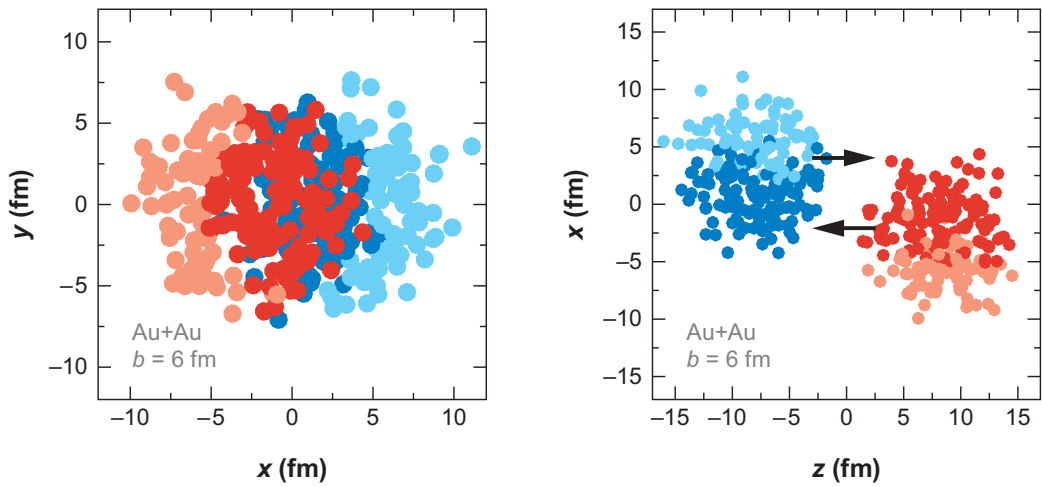


Figure 1.11: A Glauber Monte Carlo event for  $Au + Au$  at  $\sqrt{s_{NN}} = 200$  GeV with impact parameter of 6 fm viewed in the (left) transverse plane and (right) along the beam axis. Darker circles represent the participating nucleons. Taken from [75].

$$T_{AB}(\mathbf{b}) = \int T_A(\mathbf{s})T_B(\mathbf{s} - \mathbf{b})d^2s \quad (1.8)$$

170 The probability of then having  $n$  interactions between nuclei  $A$  and  $B$  is given by the binomial distribution:

$$P(n, \mathbf{b}) = \binom{AB}{n} \left[ T_{AB}(\mathbf{b})\sigma_{\text{inel}}^{\text{NN}} \right]^n \left[ 1 - T_{AB}(\mathbf{b})\sigma_{\text{inel}}^{\text{NN}} \right]^{AB-n} \quad (1.9)$$

171 where the first term is the number of combinations for finding  $n$  collisions from  $AB$  possibilities, the  
172 second term is the probability for having exactly  $n$  collisions, and the last term the probability of  $AB - n$   
173 misses. Then the total probability of an interaction between A and B is

$$\frac{d^2\sigma_{\text{inel}}^{\text{AB}}}{db^2} \equiv p_{\text{inel}}^{\text{AB}}(b) = \sum_{n=1}^{AB} P(n, \mathbf{b}) = 1 - \left[ 1 - T_{AB}(\mathbf{b})\sigma_{\text{inel}}^{\text{NN}} \right]^{AB} \quad (1.10)$$

174 Then the total cross section is given by

$$\sigma_{\text{inel}}^{\text{AB}} = \int_0^\infty 2\pi b db \left[ 1 - \left( 1 - T_{AB}(\mathbf{b})\sigma_{\text{inel}}^{\text{NN}} \right)^{AB} \right] \quad (1.11)$$

175 and  $N_{\text{coll}}$  and  $N_{\text{part}}$  are given by [77, 78]

$$N_{\text{coll}}(b) = \sum_{n=1}^{AB} n P(n, b) = AB \times T_{AB}(b)\sigma_{\text{inel}}^{\text{NN}} \quad (1.12)$$

$$N_{\text{part}}(b) = A \int T_A(\mathbf{s}) \left[ 1 - \left( 1 - T_B(\mathbf{s} - \mathbf{b})\sigma_{\text{inel}}^{\text{NN}} \right)^B \right] d^2s + B \int T_B(\mathbf{s} - \mathbf{b}) \left[ 1 - \left( 1 - T_A(\mathbf{s})\sigma_{\text{inel}}^{\text{NN}} \right)^A \right] d^2s \quad (1.13)$$

176 The correlation between  $N_{\text{coll}}$  and  $N_{\text{part}}$  can be seen in Figure 1.12

177 The charged particle multiplicity  $N_{\text{ch}}$  along with the combination of  $N_{\text{part}}$  and impact parameter  $b$  can  
178 be used to determine the centrality of a heavy ion event. An example of this is shown in Figure 1.13.

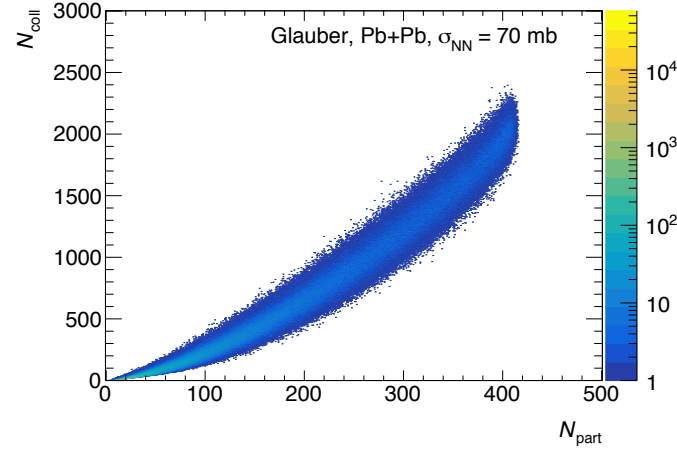


Figure 1.12: The  $N_{\text{coll}} - N_{\text{part}}$  correlation for Pb+Pb collisions at  $\sqrt{s_{\text{NN}}} = 5.02 \text{ TeV}$ . Taken from [79].

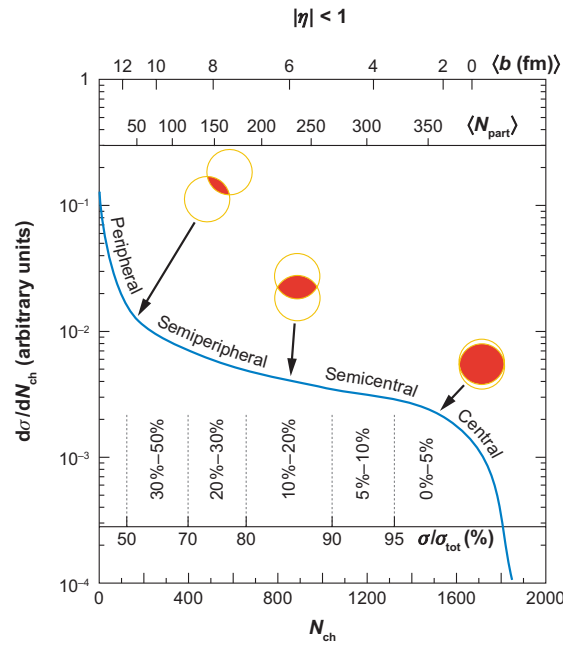


Figure 1.13: The correlation between the observable  $N_{\text{ch}}$  and  $N_{\text{part}}$  to determine the centrality distribution. Taken from [75].

## 179 1.4 Jets and Jet Quenching

180 Hard scatterings in particle collisions result in the production of highly energetic partons that form conical  
 181 sprays of hadrons called jets. A schematic of this process is shown in Figure 1.14. Jet production in a vacuum  
 182 is well described in context of perturbative QCD [80] where processes involving large momentum transfers  
 183 like high  $p_T$  hadron production can be described in terms of the parton distribution functions, scattering  
 184 cross sections, and final state fragmentation functions as shown below [81]:

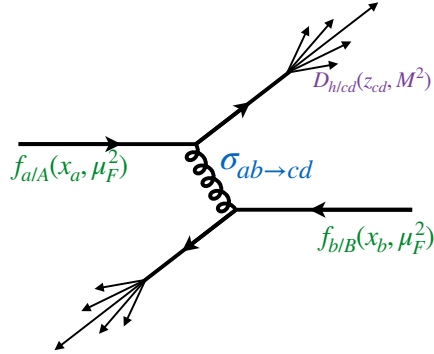


Figure 1.14: Jet production from the process  $pp \rightarrow hX$ , factorizing in terms of the parton distribution functions, scattering cross sections, and jet fragmentation functions. [81]

$$d\sigma_{pp \rightarrow hX} \approx \sum_{abjd} \int dx_a \int dx_b \int dz_j f_{a/p}(x_a, \mu_f) \otimes f_{b/p}(x_b, \mu_f) \\ \otimes d\sigma_{ab \rightarrow jd}(\mu_f, \mu_F, \mu_R) \\ \otimes D_{j \rightarrow h}(z_j, \mu_f) \quad (1.14)$$

185 where  $x_a = p_a/P_A, x_b = p_b/P_B$  are the initial momentum fractions carried by the interacting partons,  
 186  $z_j = p_h/p_j$  is the momentum fraction carried by the final observed hadron.  $f_{a/p}(x_a, \mu_f)$  and  $f_{b/p}(x_b, \mu_f)$  are  
 187 the two parton distribution functions (PDFs),  $d\sigma_{ab \rightarrow jd}(\mu_f, \mu_F, \mu_R)$  is the differential cross section for parton  
 188 scattering and  $D_{j \rightarrow h}(z_j, \mu_f)$  is the fragmentation function (FFs) for parton  $j$  to hadron  $h$ .  $\mu_f$  and  $\mu_F$  are the  
 189 factorization scales and  $\mu_R$  is the renormalization scale, and are typically taken to be the same hard scale  $Q$ .  
 190 The PDFs characterize the initial state and represent the probability of finding a parton with momentum  
 191 fraction  $x$  (shown in Figure 1.15) in the initial hadron, while the FFs describe the probability of fragmenting  
 192 to a hadron  $h$  with given kinematic properties.

193 In the case of heavy ion collisions, the jet observables can be modified due to two sources: the nuclear

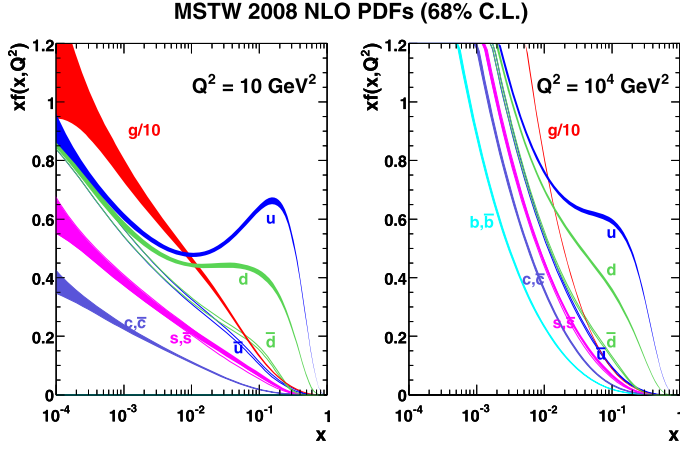


Figure 1.15: The next to leading order (NLO) PDFs at (left)  $Q^2 = 10 \text{ GeV}^2$  and (right)  $Q^2 = 10^4 \text{ GeV}^2$ . The band is the associated one-sigma (68%) confidence level uncertainty. Taken from [82]

194 PDF being distinct from a proton PDF, and the formation of the quark gluon plasma.

195 The former is collectively referred to as cold nuclear matter (CNM) effect, and can be quantified by  
196 defining a nuclear modification factor for the PDF:

$$R_a^A(x, Q^2) = \frac{f_{a/A}(x, Q^2)}{f_{a/p}(x, Q^2)} \quad (1.15)$$

197 where  $f_{a/A}$  and  $f_{a/p}$  are the nuclear and proton PDFs respectively. This  $R_a^A$  factor is determined by global  
198 fits to data from DIS measurements [83–85]. CNM effects include the following contributions:

- 199 • Shadowing: This is a destructive interference effect that reduces the interactions of a nucleon incident  
200 on a nucleus within its interior and on its back face. This effect reduces the effective number of nucleons  
201 in an inelastic interaction to  $A^{2/3}$ . For  $Q^2$  of the order of a few  $\text{GeV}^2$ , this effect dominates for  $x < 0.05$   
202 and implies  $R_a^A(x, Q^2) < 1$  [86].
- 203 • Anti-shadowing: This compensates for the shadowing effect based on the momentum sum rule, and for  
204  $Q^2$  of the order of a few  $\text{GeV}^2$  implies  $R_a^A(x, Q^2) > 1$  over the region  $0.05 < x < 0.20$ .
- 205 • EMC: The modification of the nuclear structure function was first observed by the European Muon  
206 Collaboration [87]. Recent observations have suggested that the effect is caused by short-range  
207 correlated nucleon pairs within nuclei [88]. For  $Q^2$  of the order of a few  $\text{GeV}^2$ , this effect dominates for  
208  $0.2 < x < 0.80$  and implies  $R_a^A(x, Q^2) < 1$ .

- 209 • Fermi Motion: This effect considers the motion of the nucleons within the nucleus. It results in  
 210       $R_a^A(x, Q^2) > 1$  over the  $x > 0.8$  region for  $Q^2$  of the order of a few  $\text{GeV}^2$  [89].

211 Cold nuclear matter effects are experimentally measured using  $p + A$  systems where the size and shape of  
 212 the plasma, and hence any effects thereof, are a lot smaller.

213 The second source of modification is the formation of the hot and dense quark gluon plasma. The hot  
 214 nuclear matter effects further serve as an independent confirmation that the medium formed is strongly  
 215 interacting. Jets are formed early enough that they traverse the Quark Gluon Plasma and as strongly  
 216 interacting particles, are both affected by, and affect the QGP. This interaction typically results in the jet  
 217 losing energy and forward momentum [90, 91], with the lost energy being deposited in the medium [92]. Jets  
 218 can also pick up momentum transverse to the parton direction [93]. The hot nuclear matter effects can be  
 219 considered to be a combination of collisional and radiative energy losses summarized in Figure 1.16.

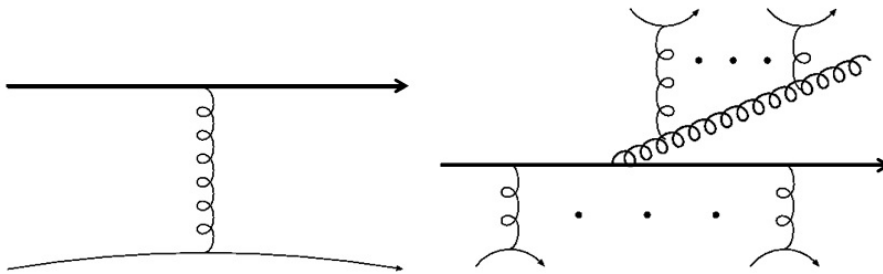


Figure 1.16: The typical diagrams for (left) collisional and (right) radiative energy losses for a parton in a hard scattering as it propagates through the QGP. Taken from [81]

- 220 • Collisional energy loss: This is a combination of elastic and inelastic collisions of the hard parton with  
 221 the constituents of the quark gluon plasma.
- 222 • Radiative energy loss: This is the larger source of parton energy loss and jet quenching. These are  
 223 modified by the presence of the plasma due to scatterings off of the plasma constituents. A variety of  
 224 radiative energy loss frameworks that have been developed include: Baier-Dokshitzer-Mueller-Peigne-  
 225 Schiff-Zakharov (BDMPS-Z) [94], Gyulassy, Levai and Vitev (GLV) [95], Amesto-Salgado-Wiedemann  
 226 (ASW) [96], Arnold-Moore-Yaffe (AMY) [97] and higher twist (HT) [98].

Both hot and cold nuclear matter effects can be described by modifying Equation 1.14 as:

$$\begin{aligned} d\sigma_{AB \rightarrow hX} &\approx \sum_{abjj'd} f_{a/A}(x_a) \otimes f_{b/B}(x_b) \\ &\otimes d\sigma_{ab \rightarrow jd}(\mu_f, \mu_F, \mu_R) \\ &\otimes P_{j \rightarrow j'} \\ &\otimes D_{h \rightarrow j'}(z_j, \mu_f) \end{aligned} \quad (1.16)$$

where the additional  $P_{j \rightarrow j'}$  describes the interaction of the hard parton with the colored medium. This is typically taken as part of the fragmentation modification as:

$$\tilde{D}_{h \rightarrow j'}(z_j, \mu_f) \approx \sum_{j'} P_{j \rightarrow j'}(p_{j'} | p_j) \otimes D_{h \rightarrow j'}(j') \quad (1.17)$$

#### 1.4.1 Jet Reconstruction

Jets can be reconstructed by clustering algorithms that take in a variety of inputs. The algorithm used in ATLAS is the anti- $k_t$  clustering algorithm [99]. This algorithm clusters soft particles around hard ones in the following manner:

- Calculate all distances  $d_{ij}$  between entities  $i$  and  $j$ , and distance  $d_{iB}$  between entity  $i$  and beam  $B$ .
- Identify the smallest distances such that for the smallest distance  $d_{ij}$ , the entities  $i$  and  $j$  are combined and return to beginning.
- If the smallest distance is  $d_{iB}$ , then take  $i$  as the jet and remove it from the list of entities and return to beginning.
- Continue the procedure till the list of items is empty.

In general the distance  $d_{ij}$  between the objects is found via the prescription

$$d_{ij} = \min(k_{Ti}^{2p}, k_{Tj}^{2p}) \frac{\Delta_{ij}^2}{R^2} \quad (1.18)$$

$$d_{iB} = k_{Ti}^{2p} \quad (1.19)$$

where  $k_{Ti}$  is the transverse momentum of particle  $i$  and  $\Delta_{ij} = \sqrt{\Delta\eta_{ij}^2 + \Delta\phi_{ij}^2}$  is the distance between particles  $i$  and  $j$  in  $\eta - \phi$  space.  $R$  the distance parameter and reflects the size of the jet being considered. In the case of the anti- $k_t$  algorithm,  $p = -1$ . Other popular clustering algorithms like  $k_t$  [100] and Cambridge/Aachen [101] use  $p = 1$  and  $p = 0$  respectively. The behavior of the different clustering algorithms is shown in Figure 1.17.

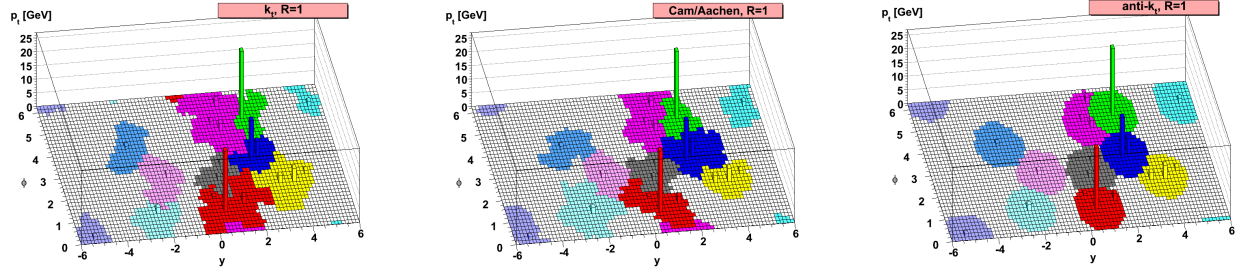


Figure 1.17: Different clustering algorithms applied to the sample parton-level event. Figure taken from [99].

The popularity of the anti- $k_t$  algorithm comes from its overcoming of two common problems: collinear and infrared safety. These are related to instabilities in the cones that are found due to soft radiation.

Figure 1.18 describes the collinear safety problem. In a collinear safe jet algorithm, the presence of a virtual loop or a collinear splitting of a central particle would not change the number of jets being reconstructed. On the other hand, while a collinear unsafe jet algorithm would not change its output with the presence of a virtual loop, a splitting in the central particle would lead to the left and right most particles forming individual seeds, implying two reconstructed jets [102].

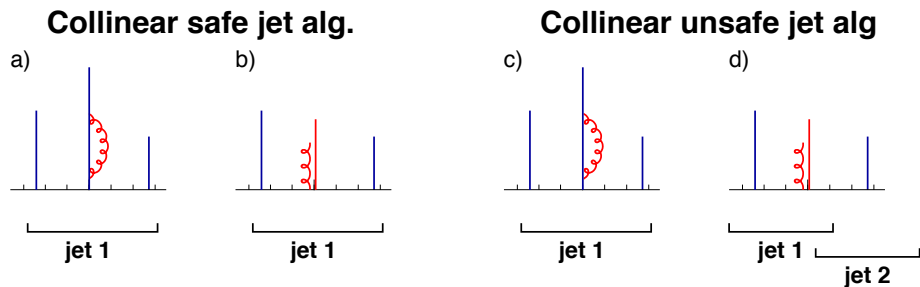


Figure 1.18: An illustration of collinear unsafe behavior. The particle  $p_T$  is proportional to the height and the horizontal axis indicates rapidity. Taken from [102].

A schematic describing infrared safety problem is shown in Figure 1.19. Here an infrared safe algorithm would use the three particles as seeds iteratively find two stable cones. An unsafe algorithm however would find three overlapping cones based on the addition of a soft seed.

For heavy ion collisions in ATLAS, the inputs to the algorithm are the  $\eta \times \phi = 0.1 \times 0.1$  calorimeter

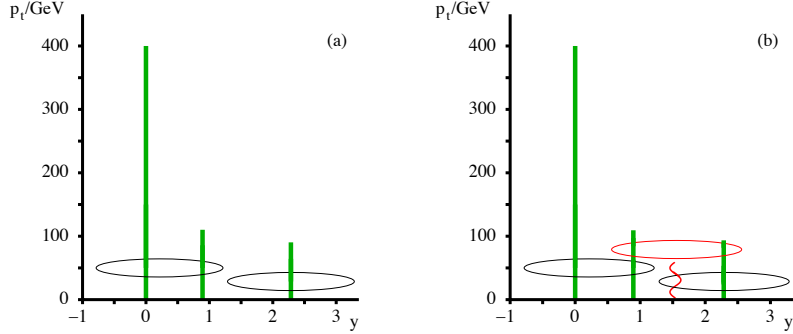


Figure 1.19: An illustration of infrared unsafe behavior. The particle  $p_T$  is proportional to the height and the horizontal axis indicates rapidity. Taken from [103].

towers. The tower energies are determined by summing up the energies of the individual calorimeter cells.  
 The anti- $k_t$  algorithm is first run with the distance parameter  $R = 0.2$ , following which an underlying event subtraction procedure is performed. A first estimate of the average underlying event energy density  $\rho_i(\eta)$  is done in 0.1 slices of  $\eta$  in each calorimeter layer  $i$  after excluding the regions that overlap with the seed jets.  
 A modulation of  $2v_2 \cos[2(\phi - \Psi_2)]$  is applied to account for the flow from the QGP and the underlying event is subtracted to give  $E_{Tj}^{\text{sub}}$ :

$$E_{Tj}^{\text{sub}} = E_{Tj} - A_j \rho_i(\eta_j) \left( 1 + 2 \sum_{n=2}^4 v_{ni} (\cos[2(\phi - \Psi_n)]) \right) \quad (1.20)$$

where  $E_{Tj}$ ,  $\eta_j$ ,  $\phi_j$  and  $A_j$  are the cell  $E_T$ ,  $\eta$ ,  $\phi$  and area for cell  $j$  in layer  $i$ . This process is done iteratively done one more time after getting new seeds with the distance parameter  $R = 0.2$  and excluding areas that are within  $\Delta R = 0.4$  of the seeds. Updated values of  $\rho'_i$  and  $v'_2$  are recalculated and used to estimate the background that is subtracted from the original cell energies. More details on this procedure can be found in [104].

# Chapter 2

## Major Jet Measurements

267 This chapter shall discuss some important experimental jet measurements that motivate the study of the  
268 main analysis in this thesis. These include the study of the jet yields, dijet asymmetry, and jet fragmentation.  
269 It shall then go on to discuss a few models that have been used to explain the data, looking in particular at  
270 the following: Effective Quenching (EQ), Soft Collinear Effective Theory (SCET), Hybrid Model, and Jet  
271 Fluid Model.

### 272 2.1 Dijet Balance: $x_J$

273 This section will discuss the dijet balance for  $R = 0.4$  jets as measured by ATLAS detector for Pb+Pb  
274 collisions at  $\sqrt{s_{\text{NN}}} = 2.76$  TeV [105]. The dijet imbalance can be expressed in terms of  $x_J$  defined as

$$x_J = \frac{p_{\text{T}2}}{p_{\text{T}1}} \quad (2.1)$$

275 where  $p_{\text{T}2}$  and  $p_{\text{T}1}$  are the transverse momenta of the two highest- $p_{\text{T}}$  jets in the event respectively. The  
276 minimum  $p_{\text{T}2}$  considered is 25 GeV and the pair of jets are separated by  $|\Delta\phi| > 7\pi/8$ . The dijet yields  
277 normalized by the number of jets and determined as  $1/N_{\text{jets}} dN/dx_J$  are presented as a function of  $x_J$  for  
278 different centrality intervals, as well as different ranges for  $p_{\text{T}1}$ . The measured distributions are further  
279 unfolded to remove detector resolution effects and allow comparison to theoretical models.

280 Figure 2.1 shows the  $x_J$  distribution for dijet pairs in  $pp$  and Pb+Pb collisions in two different centrality  
281 bins and two  $p_{\text{T}1}$  ranges. It can be seen that the dijet yields in  $pp$  are peaked at unity and become narrower  
282 for larger  $p_{\text{T}1}$  ranges. This reflects the fact that the effects of jet quenching are minimal and the higher- $p_{\text{T}}$   
283 jets are better balanced. The dijet yields in peripheral Pb+Pb collisions are similar to the distributions from  
284 the  $pp$  data, showing that the effects of quenching are smaller. On the other hand, dijet yields in central  
285 Pb+Pb collisions are significantly broadened, reflecting the maximal of jet quenching. This is consistent with  
286 the picture of the individual jets in the dijet pair traversing different lengths in the QGP and hence losing

287 different amounts of energy. In fact, the distribution for Pb+Pb data is peaked at  $x_J = 0.5$ , implying a loss  
 288 of 50% of the jet  $p_T$ .

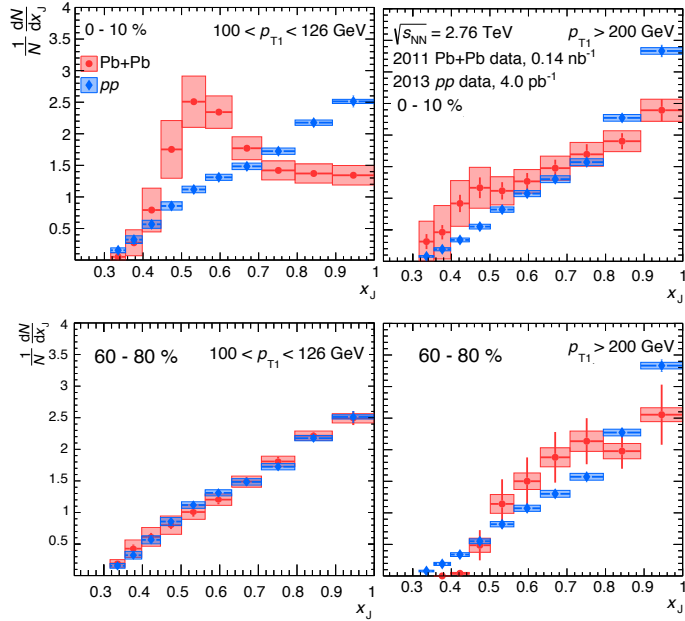


Figure 2.1: The  $1/N_{\text{jets}} dN/dx_J$  distributions for  $R = 0.4$  jets as a function of  $x_J$  for  $pp$  (blue) and  $\text{Pb+Pb}$  (red) collisions. The different panels are for (top) central and (bottom) peripheral collisions in (left)  $100 < p_{T1} < 126 \text{ GeV}$  and (right)  $p_{T1} > 200 \text{ GeV}$ . The  $pp$  data is the same in all panels. The statistical uncertainties are indicated by the bars while the boxes indicate the systematic uncertainties. Figures taken from [105].

299 Further measurements of  $R = 0.3$  jets are shown in Figure 2.2. These distributions are significantly flatter  
 300 than the ones for  $R = 0.4$  jets, an observation that is consistent with the expectation that the transverse  
 301 momenta correlation between the dijet pair is weaker for jets with smaller radii due to radiation that is  
 302 outside the nominal jet cone.

## 293 2.2 Modification of jet yields: $R_{AA}$

294 This section discusses the measurement of the inclusive jet  $R_{AA}$  as measured by the ATLAS detector for  
 295  $R = 0.4$  jets in  $\sqrt{s_{\text{NN}}} = 5.02 \text{ TeV}$   $\text{Pb+Pb}$  collisions [106].

296 While a measurement that compares the jets in a dijet system to each other as discussed in Section 2.1  
 297 can provide valuable information about how jets lose energy, it has the following limitation: If both jets lose  
 298 equal amounts of energy, the dijet yield will still be peaked at unity and no new information will be obtained.  
 299 Thus, it is useful to compare the jet yields directly between the  $pp$  and  $\text{Pb+Pb}$  systems and construct the jet  
 300  $R_{AA}$  observable. This is defined as:

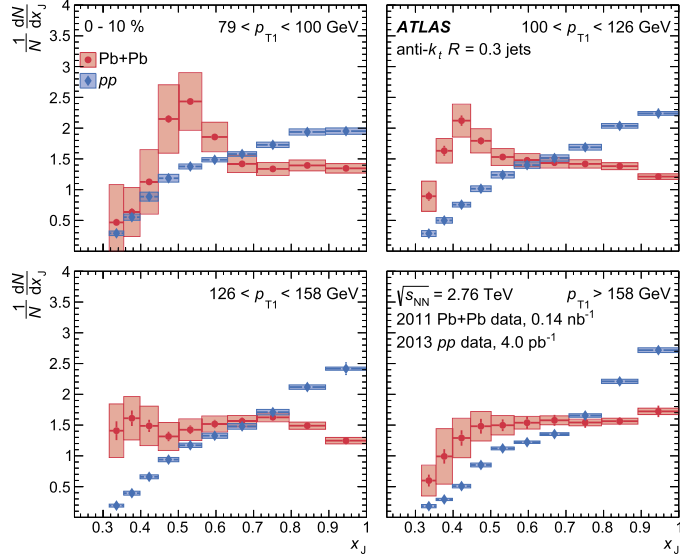


Figure 2.2: The  $1/N_{\text{jets}} dN/dx_J$  distributions for  $R = 0.3$  jets as a function of  $x_J$  in  $pp$  and central  $\text{Pb}+\text{Pb}$  collisions. The different panels are for different,  $p_{T1}$  ranges (top left to bottom right) central and (bottom) peripheral collisions. The  $\text{Pb}+\text{Pb}$  data is in red circles while the  $pp$  data is in blue diamonds and is the same in all panels. The statistical uncertainties are indicated by the bars while the boxes indicate the systematic uncertainties. Figures taken from [105].

$$R_{\text{AA}} = \frac{\frac{1}{N_{\text{evt}}} \left. \frac{d^2 N_{\text{jet}}}{dp_{\text{T}} dy} \right|_{\text{cent}}}{\langle T_{\text{AA}} \rangle \left. \frac{d^2 \sigma_{\text{jet}}}{dp_{\text{T}} dy} \right|_{\text{pp}}} \quad (2.2)$$

301 where  $T_{\text{AA}}$  is the nuclear thickness function and accounts for the geometric enhancement between  $pp$  and  
 302  $\text{Pb}+\text{Pb}$  as discussed in Section 1.3 and [75].

303 This measurement was conducted for jets in the 40–1000 GeV range in different rapidity and centrality  
 304 intervals. The jet yields in  $pp$  and  $\text{Pb}+\text{Pb}$  collisions are shown in Figure 2.3. The  $\text{Pb}+\text{Pb}$  jet yields are  
 305 scaled by the thickness function and are shown for 8 centrality intervals.

306 Figure 2.4 shows the measured inclusive jet  $R_{\text{AA}}$  as a function of jet  $p_{\text{T}}$  for different centrality bins and jet  
 307 rapidity  $|y| < 2.8$ . It can be seen that the most central collisions show a clear suppression with an  $R_{\text{AA}} \approx 0.45$   
 308 at jet  $p_{\text{T}} = 100$  GeV. The  $R_{\text{AA}}$  value slowly evolves with jet  $p_{\text{T}}$  and rises to 0.6 at jet  $p_{\text{T}} = 800$  GeV. This  
 309 modification becomes smaller for more peripheral collisions.

310 The smooth centrality dependence can be more clearly seen in Figure 2.11(a), where  $R_{\text{AA}}$  is shown as a  
 311 function of  $\langle N_{\text{part}} \rangle$  for jets the 100–126 GeV and 200–251 GeV ranges. The magnitude of the suppression is  
 312 also seen to significantly depend on jet  $p_{\text{T}}$  for  $\langle N_{\text{part}} \rangle \geq 50$ .

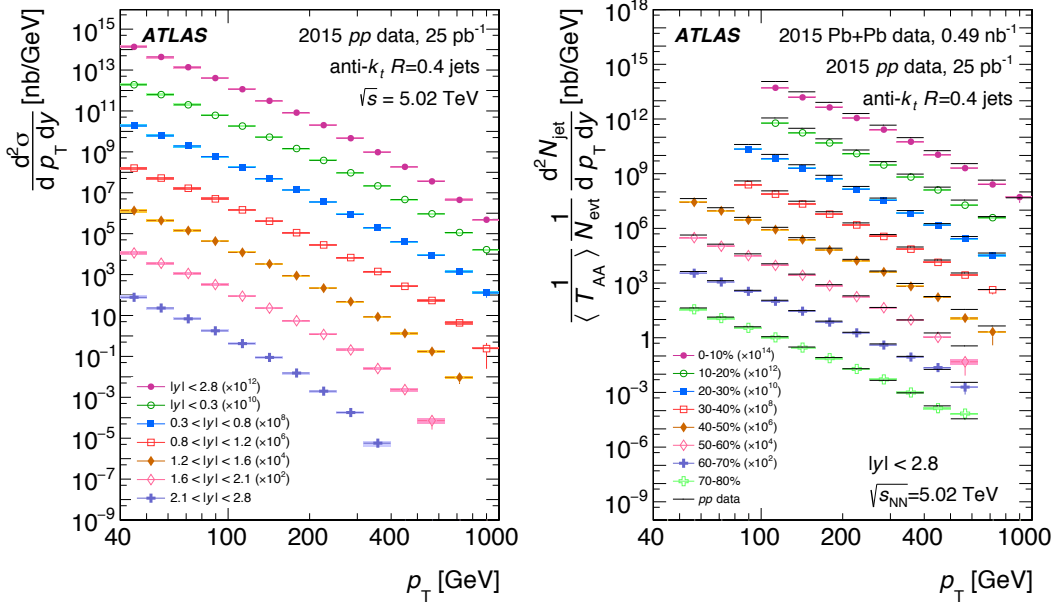


Figure 2.3: (Left) The inclusive jet cross section in  $pp$  collisions as a function of jet  $p_T$  in different  $|y|$  intervals scaled by successive powers of  $10^2$  for visibility. (Right) Per event inclusive jet yield in  $Pb+Pb$  collisions normalized by  $\langle T_{AA} \rangle$  as a function of jet  $p_T$  in different centrality intervals scaled by successive powers of  $10^2$  for visibility. The solid lines represent the cross section from  $pp$  data at the same rapidity interval scaled by the same  $10^2$  factor. Figure taken from [106].

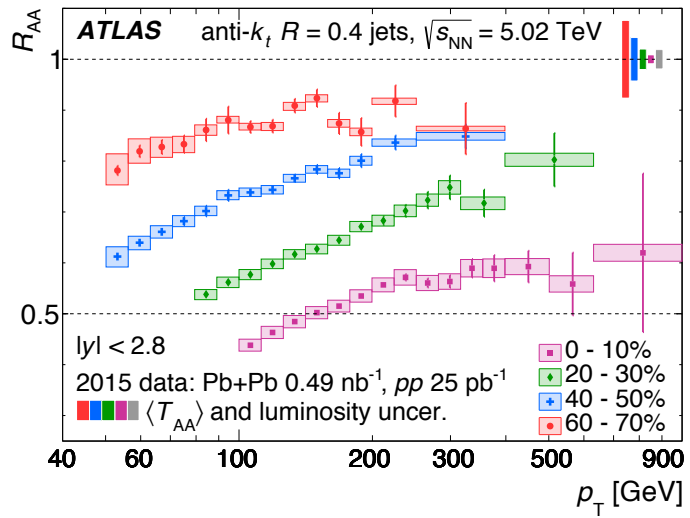


Figure 2.4: The  $R_{AA}$  distributions as a function of jet  $p_T$  for different centrality bins and jet rapidity  $|y| < 2.8$ . The error bars represent statistical uncertainties while the shaded boxes represent systematic uncertainties. Figure taken from [106].

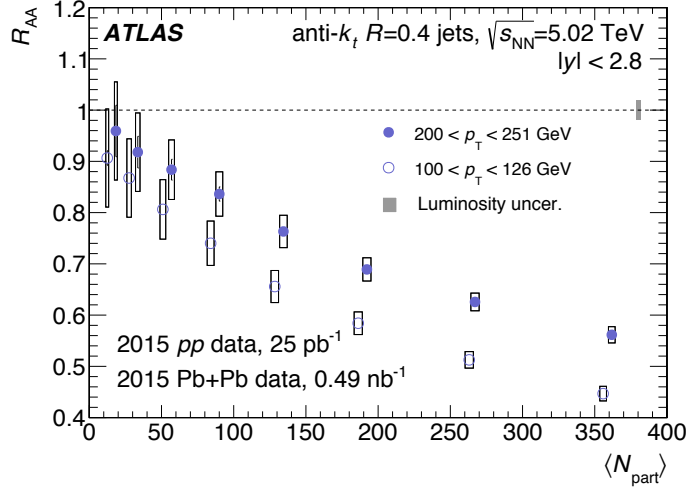


Figure 2.5: The  $R_{AA}$  distributions as a function of jet  $p_T$  for different centrality bins and jet rapidity  $|y| < 2.8$ . The error bars represent statistical uncertainties while the shaded boxes represent systematic uncertainties. Figure taken from [106].

### 313 2.3 Jet Fragmentation

314 This discussion is based on the measurement described in [107]. While measurements like  $R_{AA}$  [] and  
 315 asymmetry [] describe how much energy is lost by the jet, fragmentation measurements describe the  
 316 momentum distribution of particles associated to the jet. These can be described as:

$$D(z) = \frac{1}{N_{\text{jet}}} \frac{dn_{\text{ch}}}{dz} \quad (2.3)$$

$$D(p_T) = \frac{1}{N_{\text{jet}}} \frac{dn_{\text{ch}}}{dp_T} \quad (2.4)$$

317 where  $z = p_T \cos(\Delta R / p_T^{\text{jet}})$  and gives the charged-particle longitudinal momentum fraction relative to the jet.  
 318 Modifications to the fragmentation functions in Pb+Pb collisions can be evaluated by constructing the ratios:

$$R_{D(z)} = \frac{D(z)_{\text{Pb+Pb}}}{D(z)_{pp}} \quad (2.5)$$

$$R_{D(p_T)} = \frac{D(p_T)_{\text{Pb+Pb}}}{D(p_T)_{pp}} \quad (2.6)$$

319 This measurement is corrected for detector effects and unfolded to the particle level. This allows for  
 320 comparisons to other measurements and theoretical models. The  $D(z)$  and  $D(p_T)$  distributions are shown in

321 Figure ?? and Figure 2.6

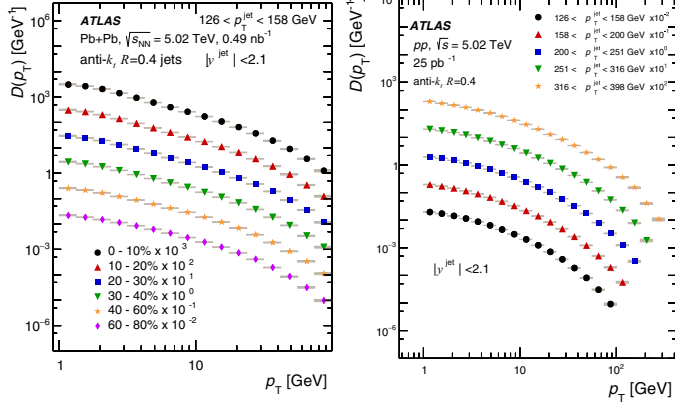


Figure 2.6: (Left) The  $D(p_T)$  distributions in  $pp$  as a function of charged-particle  $p_T$  for different  $p_T^{\text{jet}}$  selections and for jet rapidity  $|y| < 2.1$ . (Right) The  $D(p_T)$  distributions in  $\text{Pb}+\text{Pb}$  as a function of charged-particle  $p_T$  for different centrality selections and for jet rapidity  $|y| < 2.1$ . The error bars represent statistical uncertainties while the shaded boxes represent systematic uncertainties. Figure taken from [107].

322 The modifications to the  $D(z)$  distributions are shown in Figure 2.7. It can be seen that there is an excess  
 323 of particles with low  $z$  and high  $z$ . These are particles that carry either a small or a large fraction of energy  
 324 of the jet  $p_T$ . There is an associated depletion for particles with intermediate  $z$ . These modifications become  
 325 smaller for more peripheral collisions. The  $p_T^{\text{jet}}$  dependence of the  $R_{D(z)}$  and  $R_{D(p_T)}$  distributions can be  
 326 seen in Figure 2.8. This dependence can give insight into the modification of the fragmentation functions,  
 327 with any scaling with  $z$  indicating a change in the fragmentation pattern, while a scaling with  $p_T$  reflecting an  
 328 effect from the medium itself. The low momentum excess in the  $R_{D(p_T)}$  distributions seen in Figure 2.8 can  
 329 be further studied by integrating over that region. Then the extra number of particles in  $\text{Pb}+\text{Pb}$  compared  
 330 to  $pp$  is given by:

$$N_{\text{ch}} = \int_{p_{T_{\min}}}^{p_{T_{\max}}} \left( D(p_T)_{\text{Pb}+\text{Pb}} - D(p_T)_{pp} \right) dp_T \quad (2.7)$$

331 where  $p_{T_{\min}} = 1 \text{ GeV}$  and  $p_{T_{\max}} = 4.2 \text{ GeV}$ . The  $N_{\text{ch}}$  distributions can be seen in Figure 2.9. It can be  
 332 clearly seen that the size of the excess increases as a function of  $p_T^{\text{jet}}$ , growing from about 1.5 to 2.5 extra  
 333 particles in the most central  $\text{Pb}+\text{Pb}$  collisions. This excess is even seen in the peripheral  $\text{Pb}+\text{Pb}$  collisions,  
 334 though it is a lot smaller and ranges from 0.2 to 0.5 extra particles.

335 The modifications to the  $D(z)$  distributions have also been compared to a variety of models, including  
 336 the Effective Quenching model [108], the Soft Collinear Effective Theory [109, 110], and the Hybrid Model

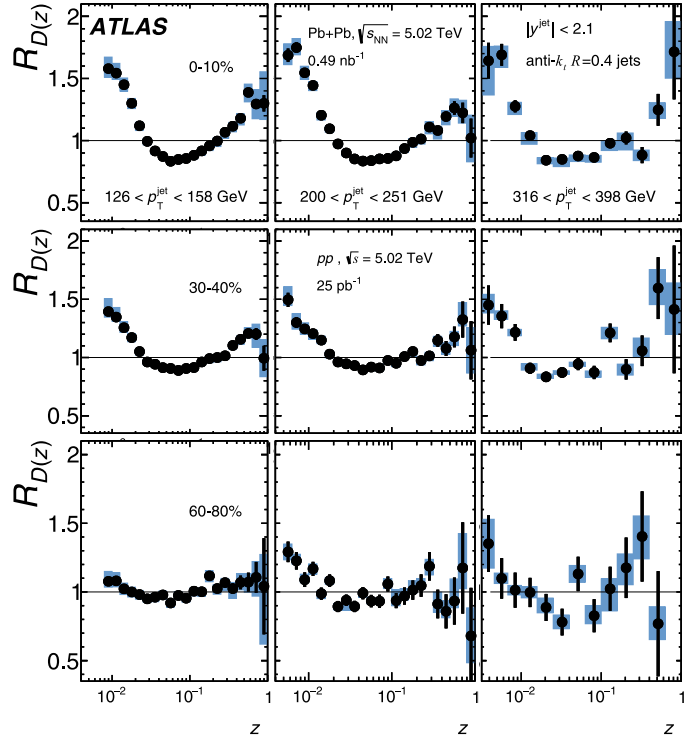


Figure 2.7: The modifications to the  $D(z)$  distributions in  $\text{Pb}+\text{Pb}$  compared to  $pp$  as a function of charged-particle  $z$  for different  $p_T^{\text{jet}}$  selections (left to right) and different centrality selections (top to bottom) for jet rapidity  $|y| < 0.3$ . The error bars represent statistical uncertainties while the shaded boxes represent systematic uncertainties. Figure taken from [107].

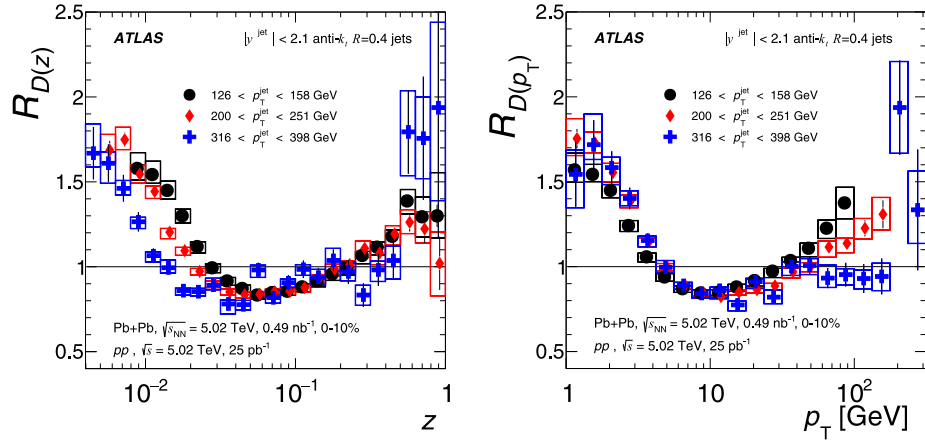


Figure 2.8: The  $p_T^{\text{jet}}$  dependence of the  $R_{D(z)}$  (left) and  $R_{D(p_T)}$  (right) distributions in 0–10% central  $\text{Pb}+\text{Pb}$  compared to  $pp$  collisions. The error bars represent statistical uncertainties while the shaded boxes represent systematic uncertainties. Figure taken from [107].

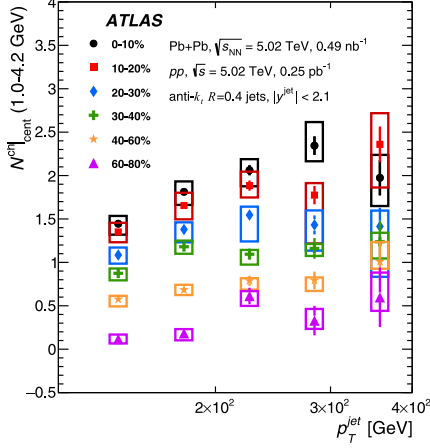


Figure 2.9: The number of extra particles that carry  $1 < p_T < 4$  GeV in  $\text{Pb}+\text{Pb}$  compared to  $pp$ . The different colors represent different centrality selections. The error bars represent statistical uncertainties while the shaded boxes represent systematic uncertainties. Figure taken from [107].

<sup>337</sup> [111]. These comparisons are shown in Figure 2.10. It can be seen that

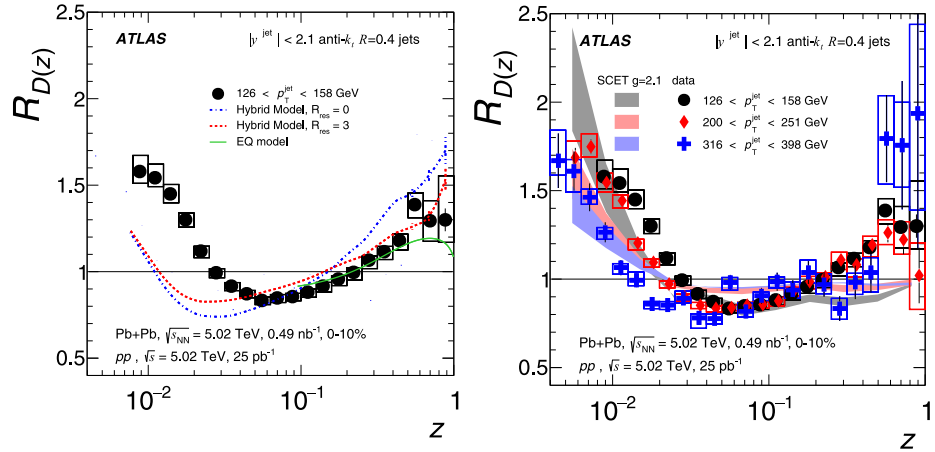


Figure 2.10: The  $R_{D(z)}$  distributions compared to the EQ and Hybrid models (left) and SCET (right). The error bars represent statistical uncertainties while the shaded boxes represent systematic uncertainties. Figure taken from [107].

## <sup>338</sup> 2.4 Effective Quenching

<sup>339</sup> This discussion is based on the model introduced in Ref. [108]. This phenomenological model emphasizes  
<sup>340</sup> the jet  $p_T$  dependence of the quark to gluon fraction and the difference between quark-jet and gluon-jet  
<sup>341</sup> quenching. It uses an “extended” power law parameterization of the high- $p_T$  hadron spectra coupled with a

342 quenching that is based on a non-constant fractional energy loss. This model considers the different color  
343 charges carried by quarks and gluons and their different splitting functions, and assumes that gluon jets lose  
344 energy at a rate 9/4 times higher than quark jets. The key assumption of the model are:

- 345 • The energy lost by a jet is radiated at large angles and does not appear within the jet cone. This is  
346 backed by [112].
- 347 • The fragmentation pattern of the jet is unaffected by the presence of the QGP i.e. they fragment as  
348 they would in a vacuum. This is motivated by the idea that the QGP is unable to resolve the internal  
349 jet structure and is supported by [113, 114].

350 The model uses the following extended power-law parameterization to describe the high- $p_T$  jet spectra:

$$\frac{dn}{dp_T^{\text{jet}}} = A \left( \frac{p_{T0}}{p_T^{\text{jet}}} \right)^{n+\beta \log(p_T^{\text{jet}}/p_{T0})} \quad (2.8)$$

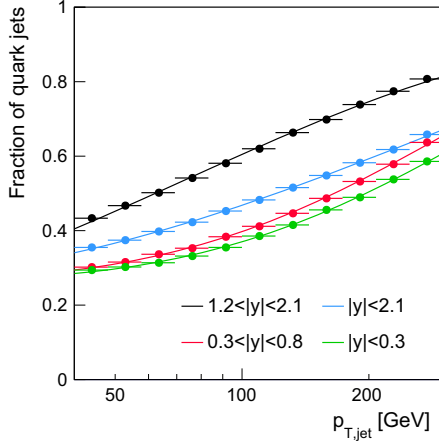
351 where  $p_{T0}$  is a reference transverse momentum at which  $A = dn/dp_T^{\text{jet}}$ ,  $\beta$  is the logarithmic derivative of  
352  $dn/dp_T^{\text{jet}}$  at  $p_T^{\text{jet}} = p_{T0}$ . Then considering the different quark and gluon fractions as  $f_{q0}$  and  $f_{g0} = 1 - f_{q0}$   
353 respectively, the combined spectrum for quarks and gluons can be written as:

$$\frac{dN}{dp_T^{\text{jet}}} = A \left[ f_{q0} \left( \frac{p_{T0}}{p_T^{\text{jet}}} \right)^{n_q + \beta_q \log(p_T^{\text{jet}}/p_{T0})} + (1 - f_{q0}) \left( \frac{p_{T0}}{p_T^{\text{jet}}} \right)^{n_g + \beta_g \log(p_T^{\text{jet}}/p_{T0})} \right] \quad (2.9)$$

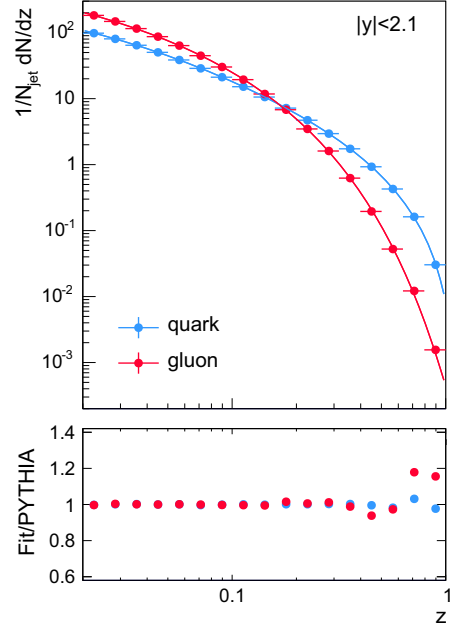
$$f_q(p_T^{\text{jet}}) = \frac{1}{1 + \left( \frac{1 - f_{q0}}{f_{q0}} \right) \left( \frac{p_{T0}}{p_T^{\text{jet}}} \right)^{\Delta n + \Delta \beta \log(p_T^{\text{jet}}/p_{T0})}} \quad (2.10)$$

354 where  $\Delta n = n_g - n_q$  and  $\Delta \beta = \beta_g - \beta_q$ . The  $p_T$  dependence of the quark fraction along with the fit is shown  
355 in Figure 2.11(a). The fragmentation functions can also be determined using final-state charged hadrons  
356 within a  $R = 0.4$  jet cone. These are fit to the form  $D(z)$ , with fits for the quark and gluon fragmentation  
357 shown in Figure 2.11(b).

$$D(z) = a \times \frac{(1 + dz)^b}{(1 + ez)^c} \times e^{-fz} \quad (2.11)$$



(a) The jet quark fraction as a function of  $p_T^{\text{jet}}$  in different rapidity bins. The points are from PYTHIA8 simulations and the lines are fits to Equation 2.10.



(b) A comparison of the PYTHIA8 quark and gluon fragmentation. The solid lines are the fits from The jet quark fraction as a function of  $p_T^{\text{jet}}$  in different rapidity bins. The points are from PYTHIA8 simulations and the lines are fits to Equation 2.11.

Figure 2.11: Fits to quark fractions and fragmentation functions from PYTHIA8. Figure taken from [108]

358 For the quenched spectra, this model assumes a non-constant fractional shift given below as  $S$ . This  
 359 approach is based on [115] and is used because of the inability of the constant fractional shift to explain the  
 360 jet  $p_T$  dependence of measured  $R_{\text{AA}}$ .

$$S = s' \left( \frac{p_T^{\text{jet}}}{p_{T0}} \right)^\alpha \quad (2.12)$$

361 where  $\alpha$  is an undetermined parameter and  $s'$  is the shift for a jet with  $p_T^{\text{jet}} = p_{T0}$ . This gives the following  
 362 quenched high- $p_T$  hadron spectra:

$$\begin{aligned} \frac{dN_Q}{dp_T^{\text{jet}}} = A & \left[ f_{q0} \left( \frac{p_{T0}}{p_T^{\text{jet}} + S_q} \right)^{n_q + \beta_q \log((p_T^{\text{jet}} + S_q)/p_{T0})} \left( 1 + \frac{dS_q}{dp_T^{\text{jet}}} \right) \right. \\ & \left. + (1 - f_{q0}) \left( \frac{p_{T0}}{p_T^{\text{jet}} + S_g} \right)^{n_g + \beta_g \log((p_T^{\text{jet}} + S_g)/p_{T0})} \left( 1 + \frac{dS_g}{dp_T^{\text{jet}}} \right) \right] \end{aligned} \quad (2.13)$$

363 Where the  $(1 + dS/dp_T^{\text{jet}})$  term is a Jacobian to preserve the number of jets. Then the  $R_{\text{AA}}$  can be written as:

$$R_{\text{AA}} = f_q \left( \frac{1}{1 + S_q/p_T^{\text{jet}}} \right)^{n_q + \beta_q \log((p_T^{\text{jet}} + S_q)/p_{T0})} \frac{p_{T0}}{p_T^{\text{jet}}} \left( 1 + \frac{dS_q}{dp_T^{\text{jet}}} \right) \times \quad (2.14)$$

$$(1 - f_q) \left( \frac{1}{1 + S_g/p_T^{\text{jet}}} \right)^{n_g + \beta_g \log((p_T^{\text{jet}} + S_g)/p_{T0})} \frac{p_{T0}}{p_T^{\text{jet}}} \left( 1 + \frac{dS_g}{dp_T^{\text{jet}}} \right) \quad (2.15)$$

364 where the flavor fraction is given by Equation 2.10. These can be fit to the measured ATLAS  $R_{\text{AA}}$  data as  
 365 shown in Figure 2.13(a) and the parameters  $s'$  and  $\alpha$  can be extracted as shown in Figure 2.12.

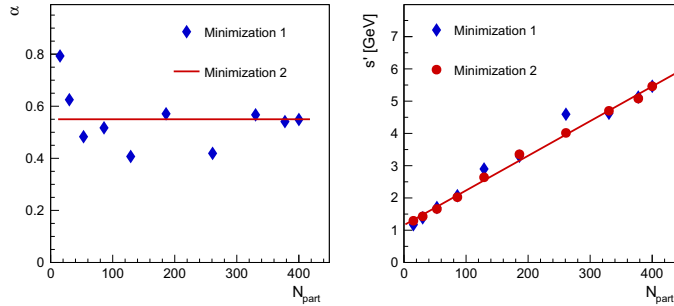
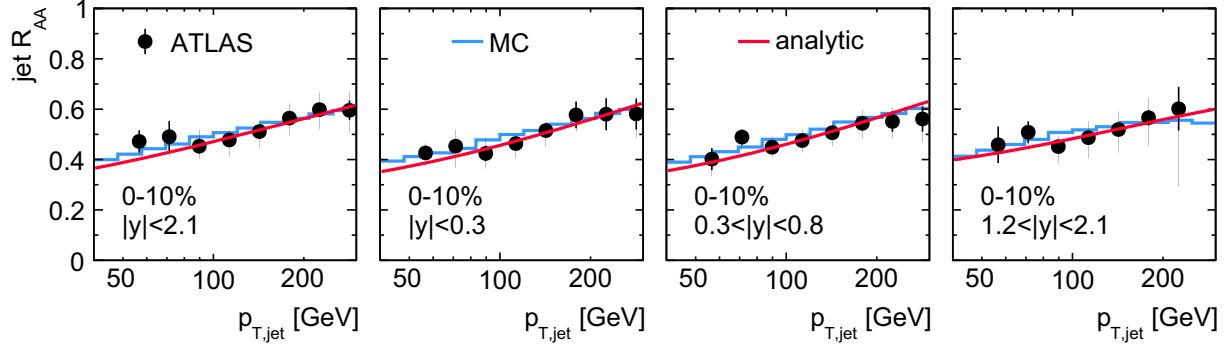
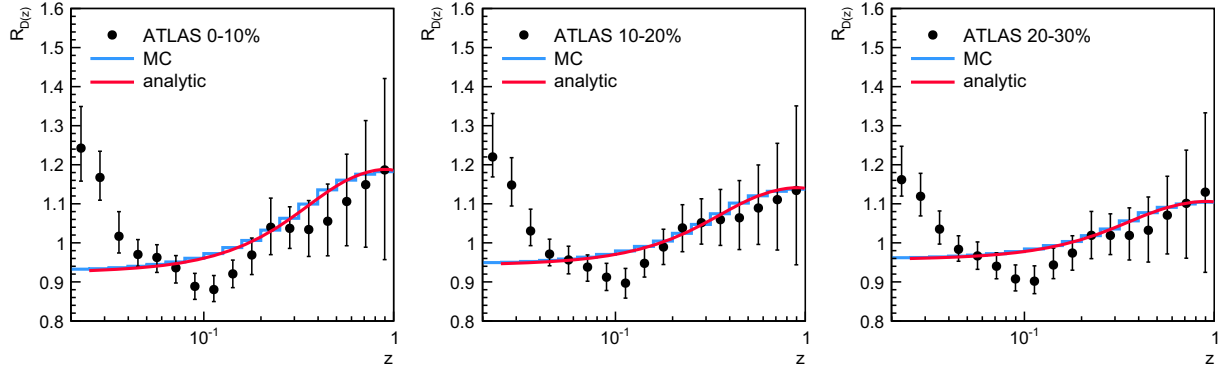


Figure 2.12: The extracted values of  $\alpha$  and  $s'$  as a function of  $N_{\text{part}}$ . The first minimization shows fluctuations for  $\alpha$  around 0.55, which was then fixed for the second minimization to give an  $s'$  that linearly depends on  $N_{\text{part}}$ . Figure taken from [108]

366 It can be seen that the analytic fits and the MC are in good agreement. While the fits agree with the data  
 367 by definition, the robustness of the model can be seen in that it describes the data with a single value for  $\alpha$   
 368 and a simple centrality dependent shift constant  $s'$ . Fits to the  $D(z)$  distributions are shown in Figure 2.13(b)  
 369 and it can be seen that while the MC and analytic calculation agree well with each other, they are only  
 370 able to qualitatively capture some features of the data. The enhancement at high  $z$  can be explained by an  
 371 increased quark content of the jet spectrum and subsequent differential quenching for quark and gluon jets.  
 372 The low  $z$  enhancement on the other hand can be considered to be a result of a gluon radiation within the  
 373 jet or a wake from the medium itself.



(a) A comparison of the  $R_{AA}$  as measured by ATLAS for central Pb+Pb collisions in [116], a MC calculation (blue) and the analytic calculation (red) in the EQ model with the extended power-law parameterization and a non-constant fractional energy loss. The different panels are different rapidity intervals.



(b) A comparison of the  $R_{D(z)}$  as measured by ATLAS in [117], a MC calculation (blue) and the analytic calculation (red) in the EQ model with the extended power-law parameterization and a non-constant fractional energy loss. The different panels are different centrality intervals.

Figure 2.13: A comparison of measured data, MC, and the analytic calculation of the EQ model. Figure taken from [108]

## 374 2.5 Jet Fluid model

375 This discussion is based on the model introduced in Ref. [118]. This model considers the evolution of the jet  
 376 and QGP in a coupled manner, considering the energy and transverse momentum exchange between them.  
 377 In this picture, both the jet and medium are allowed to modify each other; the jet is modified via collisional  
 378 and radiative processes while the medium evolves hydrodynamically and is modified because it picks up the  
 379 energy lost by the jet.

380 The time evolution of the jet is given

$$f_i(\omega_i, k_{\text{T}i}^2, t) = \frac{dN_i(\omega_i k_{\text{T}i}^2, t)}{d\omega_i dk_{\text{T}i}^2} \quad (2.16)$$

381 where  $i$  is the type of parton,  $\omega_i$  is its energy, and  $k_{\text{T}}^2$  is its transverse momentum with respect to the jet axis.

382 Then the transport equations can be written in terms of :

$$\frac{df_j}{dt} = \hat{e}_j \frac{\partial f_j}{\partial \omega_j} + \frac{1}{4} \hat{q}_j \nabla_{k_{\text{T}}}^2 f_j \quad (2.17)$$

$$+ \sum_i \int d\omega_i dk_{\text{T}i}^2 \frac{d\tilde{\Gamma}_{i \rightarrow j}}{d\omega_j dk_{\text{T}j}^2 dt} f_i \quad (2.18)$$

$$- \sum_i \int d\omega_i dk_{\text{T}i}^2 \frac{d\tilde{\Gamma}_{j \rightarrow i}}{d\omega_{ij} dk_{\text{T}i}^2 dt} f_i \quad (2.19)$$

(2.20)

383 where the first term is the collisional energy loss, the second term is the transverse momentum broadening,  
 384 and the last two terms are the medium induced gain and loss radiative processes respectively. The splitting  
 385 processes are given by:

$$\frac{d\Gamma_{i \rightarrow j}}{d\omega_j dk_{\text{T}j}^2 dt} = \frac{2\alpha_S}{\pi} \hat{q}_g \frac{x P_{i \rightarrow j}(x)}{\omega_j k_{\text{T}j}^4} \sin^2 \left( \frac{t - t_i}{2\tau_f} \right) \quad (2.21)$$

386 where  $P_{i \rightarrow j}$  is the vacuum splitting function for  $i \rightarrow j$  with  $\omega_j$  being the energy of the radiated parton,  $\tau_f$  is  
 387 the formation time of the radiated parton, and  $k_{\text{T}j}$  is the transverse momentum of the radiated parton with  
 388 respect to the parent parton. These transport Equations 2.17 can be solved numerically and agree with  $R_{\text{AA}}$   
 389 measurements [116, 119, 120]. The effects of the medium are included by considering the energy-momentum

390 conservation of the jet-QGP system  $\partial_\mu [T_{\text{QGP}}^{\mu\nu} + T_{\text{jet}}^{\mu\nu}] = 0$ . Then the source term  $J^\nu(x)$  that describes the  
 391 energy transfer between the jet and the medium can be defined as  $J^\nu(x) \equiv -\partial_\mu T_{\text{jet}}^{\mu\nu}$ , making the QGP  
 392 evolution being given by

$$\partial_\mu T_{\text{QGP}}^{\mu\nu} = j^\nu \quad (2.22)$$

393 which characterizes the energy-momentum transfer between the jet and the QGP.

394 An important component of this model is the flow induced by jets. A snapshot of this is shown in  
 395 Figure 2.14, where the evolution of the energy density of the medium can be seen in a sample event. A single  
 396 jet travels through the QGP, and can be clearly seen in the lower panels after the energy of the medium has  
 397 been subtracted out. The V shaped feature seen is the mach cone that is induced by the parton as it moves  
 398 faster than the medium sound velocity.

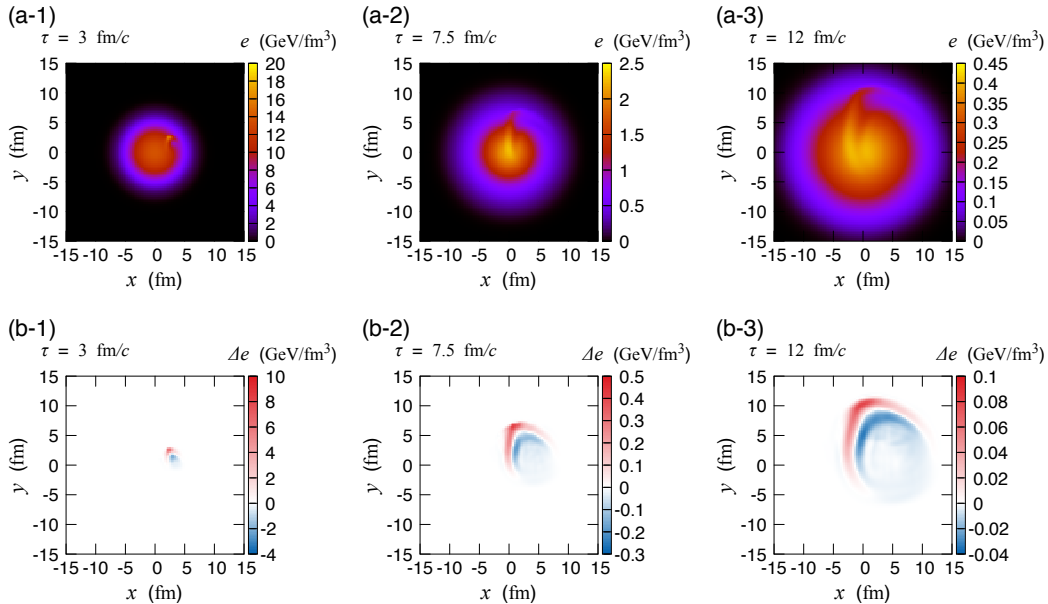


Figure 2.14: (Top) The time evolution of the energy density of the quark gluon plasma with a jet propagating through it. (Bottom) The time evolution of the energy density in the event after the energy density of the QGP has been subtracted out. Figure taken from [118].

399 The final jet energy has two components: the jet shower, and the hydrodynamic response. The former  
 400 as discussed above comprises of the collisional energy loss, momentum broadening, and medium induced  
 401 radiation. The latter includes the energy lost from the jet shower that thermalizes into the medium and  
 402 induces conical flow, some of which is still in the jet cone. This compensates some of the energy lost in the

shower and can be seen in Figure 2.15. While the absolute amount of energy lost increases as a function of initial jet energy, the fractional energy loss decreases. Furthermore there is a cone size dependence once the hydrodynamic contributions are included. This is a result of the jet being highly collimated, such that while an increase in the size does not change the energy much, it does affect the hydrodynamic contribution from the medium.

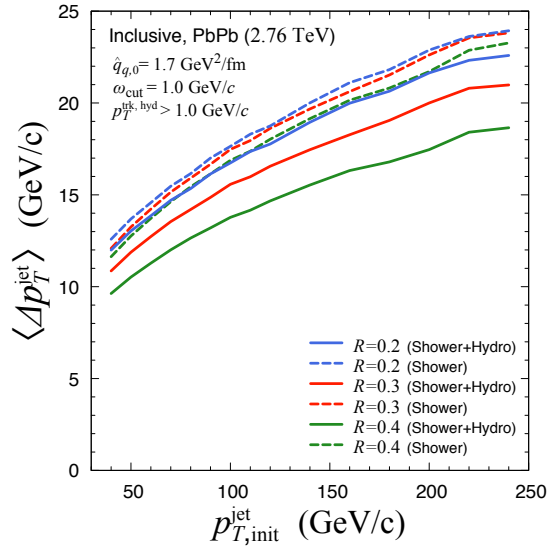


Figure 2.15: (Top) The energy lost by a jets of different radii as a function of their initial energy in central Pb+Pb collisions at  $\sqrt{s_{\text{NN}}} = 2.76$  TeV. Figure taken from [118].

The  $R_{\text{AA}}$  distributions constructed with this model and compared to data from CMS [119] are shown in Figure 2.16. Including the hydrodynamic contribution decreases the energy loss, hence increasing the  $R_{\text{AA}}$  value and inducing a cone size dependence to the  $R_{\text{AA}}$ .

The internal structure of the jet, i.e. how energy is spread within it, can be investigated using the jet shape variable, defined as a per-jet quantity as:

$$\rho_{\text{jet}} = \frac{1}{N_{\text{jet}}} \sum_{\text{jet}} \left[ \frac{1}{p_{\text{T}}^{\text{jet}}} \frac{\sum_{\text{trk}} p_{\text{T}}^{\text{ch}}}{\delta r} \right] \quad (2.23)$$

where the sum is over all jets and for all tracks around a jet in an annulus with mean radius  $r$  from the jet axis. The modification in the jet structure then can be defined as:

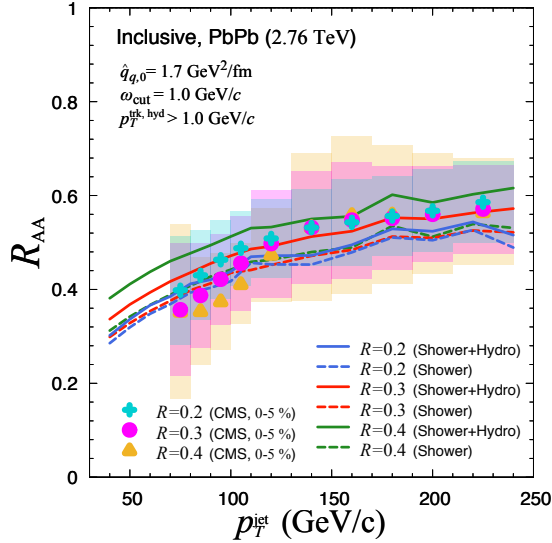


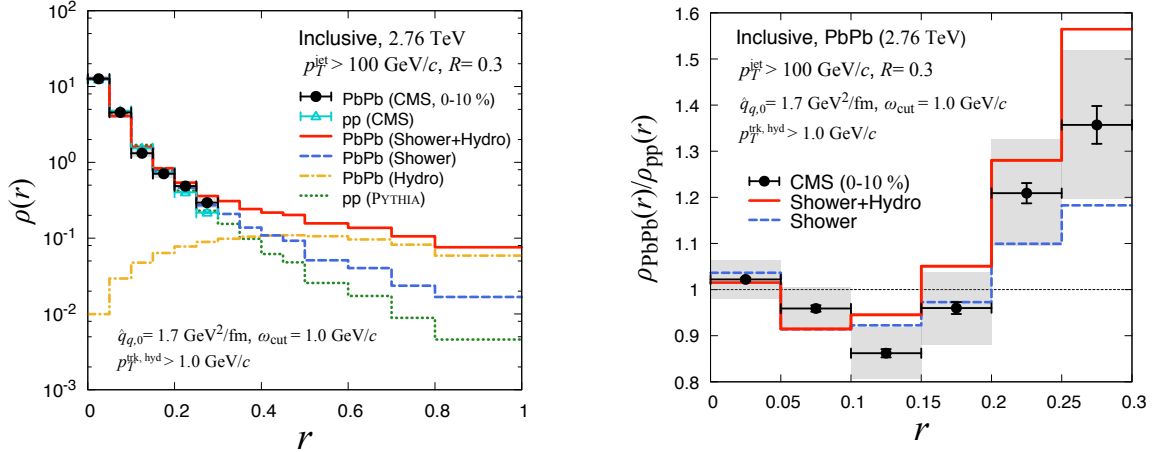
Figure 2.16: The nuclear modification factor  $R_{AA}$  as a function of jet  $p_T$  as determined by the Jet-Fluid model and compared to the data measured by CMS [119]. The different colors represent different sized jets, with the dashed lines showing the modeled  $R_{AA}$  without the hydro-contribution. There is good agreement within the large uncertainties in the data. Figure taken from [118].

$$R_{AA}^\rho = \frac{\rho_{AA}(r)}{\rho_{pp}(r)} \quad (2.24)$$

415 A comparison of the jet shape variable  $\rho$  and its modification  $R_{AA}^\rho$  to data measured by CMS is shown in  
 416 Figure 2.17. The individual shower and hydro contributions are seen in Figure 2.17(a). These indicate that  
 417 the shower contribution to the jet shape variable falls steeply as a function of distance from the jet axis  
 418 while the hydro contribution is fairly constant at large distances. This is because the energy loss from the  
 419 shower is carried away by the jet induced flow to large angles. The  $R_{AA}^\rho$  distribution in Figure 2.17(b), shows  
 420 that the core is largely unmodified while the outer part of the jet is broadened. The hydro-contribution  
 421 mainly has an effect at larger distances from the jet axis. This is consistent with the cone-size dependence  
 422 seen in Figure 2.15.

## 423 2.6 Hybrid Model

424 This discussion is based on the work in Refs. [111, 122, 123] and describes jet quenching using a hybrid  
 425 strong/weak model. It uses perturbative QCD to describe the weakly coupled hard process of jet production  
 426 and holographic calculations of the energy loss of energetic probes to model the strong coupling between the



(a) The jet shape as measured by CMS for  $pp$  and central  $Pb+Pb$  collisions [121] compared to the Jet Fluid model. The shower (blue) and hydro (orange) contributions to the jet shape are highlighted.

(b) The modification of the jet shape between  $pp$  and  $Pb+Pb$  as measured by CMS [121] and compared to the Jet Fluid model. The dashed line shows the modeled modification without the hydro-contribution.

Figure 2.17: Fits to CMS data. Figures taken from [118].

427 probe and the plasma [124, 125]. This is a combination of approaches that focus on the following extreme  
 428 limits: a weakly coupled system at unrealistically high temperatures that can be treated perturbatively  
 429 [126, 127] and a system where the coupling constant is large at all energy scales and Gauge/string duality is  
 430 applicable [128].

431 In this model, the jet evolves in space time with the lifetime of the parton in the shower being given by  
 432 [129].

$$\tau = 2 \frac{E}{Q^2} \quad (2.25)$$

433 where  $Q$  is its virtuality and  $E$  its energy. This evolution is unaffected before the proper time at which the  
 434 plasma hydrodynamizes,  $\tau_{\text{hydro}} = 0.6$  fm. After this time, the jet-plasma interaction comes into play and the  
 435 fragments evolve with the energy loss as:

$$\frac{1}{E_{\text{in}}} \frac{dE}{dx} = -\frac{4}{\pi} \frac{x^2}{x_{\text{stop}}^2} \frac{1}{\sqrt{x_{\text{stop}}^2 - x^2}} \quad (2.26)$$

436 where  $E_{\text{in}}$  is the initial energy of the parton prior to any quenching and  $x_{\text{stop}}$  is its stopping distance (jet  
 437 thermalization distance). The stopping distance can be written as:

$$x_{\text{stop}} = \frac{1}{2\kappa_{\text{sc}}} \frac{E_{\text{in}}^{1/3}}{T^{4/3}} \quad (2.27)$$

438 where  $\kappa_{\text{sc}}$  is a dimensionless free parameter associated to the strong coupling and is used to fit to the  
 439 data. The energy loss is characterized by the strong  $x^2$  dependence for  $x \ll x_{\text{stop}}$ . Furthermore, when  $x$  is  
 440 comparable to  $x_{\text{stop}}$ ,  $dE/dx$  depends nontrivially on  $E_{\text{in}}$  and  $x$ , diverging for  $x \rightarrow x_{\text{stop}}$  and  $E \rightarrow 0$ . The  
 441 shower is then embedded into a hydrodynamic description of the QGP from Ref. [130], and the energy  
 442 loss expressions are integrated for each parton, from the time it is produced to the time that it splits. The  
 443 splitting probabilities are taken to be independent of the medium, depending only on the initial energy of the  
 444 daughter partons. These further lose energy as they propagate through the QGP and split. Then the total  
 445 energy lost by a parton is dependent on the history of splitting and propagation of its parents, grandparents  
 446 and so on and so forth.

447 The partons further experience kicks transverse to their direction of motion, a phenomena called transverse  
 448 momentum broadening. This effect is mainly experienced by softer partons that are much more affected  
 449 by the angular narrowing effects of energy loss, making most measured observables insensitive to the size  
 450 of this kick. This is directly related to wider jets losing more energy than narrower ones. The wake left  
 451 in the medium from the partons depositing momentum in the QGP as they propagate through it lends a  
 452 non-trivial impact to the model predictions. This wake moves in the direction of the jet and is impossible to  
 453 separate out in experiments, making its inclusion to any model vital. This wake results in a perturbation  
 454 to the hydrodynamic background, resulting in corrections to the final state hadron spectra. This effect is  
 455 particularly important for jet substructure observables like jet fragmentation and jet shapes [123].

456 A screening effect recently included in the hybrid model is based considering the resolving power of the  
 457 QGP [122]. As depicted in Figure 2.18, the QGP will only resolve daughter partons of a splitting after they  
 458 are separated by a certain distance  $L_{\text{res}}$ . It is only after they are resolved that they will be allowed them to  
 459 lose energy independent of each other. This delayed quenching results in an enhancement of softer partons at  
 460 larger angles from the jet axis compared to the case where the daughter partons are resolved immediately  
 461 after they split from the parent parton. The  $L_{\text{res}}$  parameter has the constraint  $1/(\pi T) < L_{\text{res}} < 2/(p_{\text{T}} T)$   
 462 based on the Debye screening length for the plasma, i.e. the length at which the QGP is able to resolve and  
 463 screen color charges.

464 The free parameter  $\kappa_{\text{sc}}$  is determined by fitting to jet  $R_{\text{AA}}$  data from CMS [119] as shown in Figure 2.19.  
 465 It can be seen that including the  $L_{\text{res}}$  parameter does not really affect the jet  $R_{\text{AA}}$  prediction. The dependence

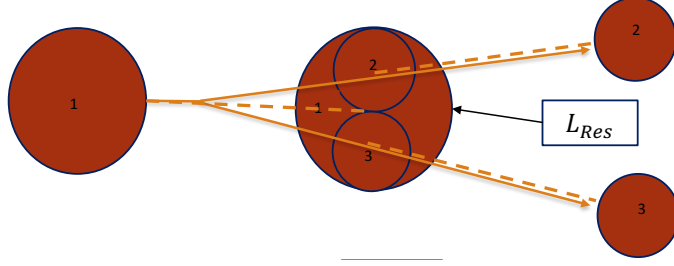


Figure 2.18: A schematic illustrating the resolving power of the QGP. The daughter partons 2 and 3 that come from 1 need to be separated by  $L_{\text{res}}$  before they are treated individually by the plasma. Prior to that separation, they are treated as one effective parton. Figure taken from [122].

466 of the  $R_{AA}$  on the size of the jet radius can be seen. This is consistent with the expectation that wider jets  
 467 lose more energy.

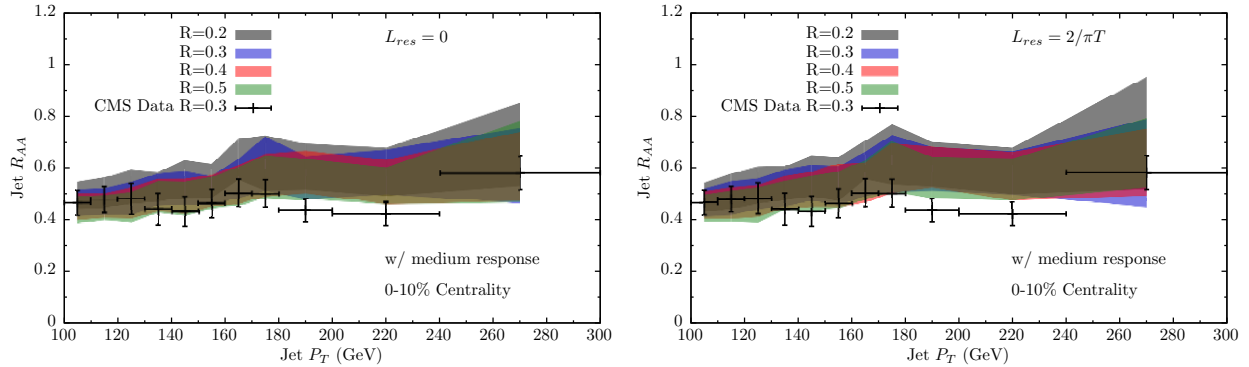
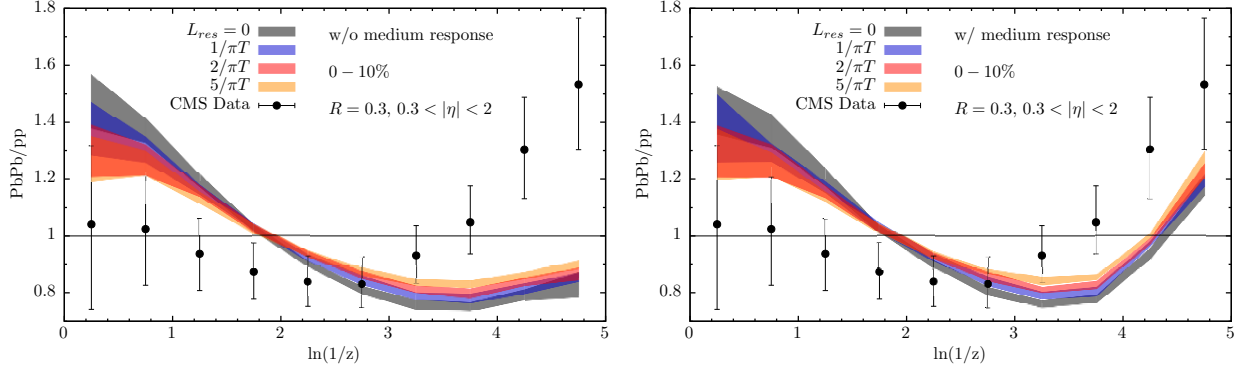


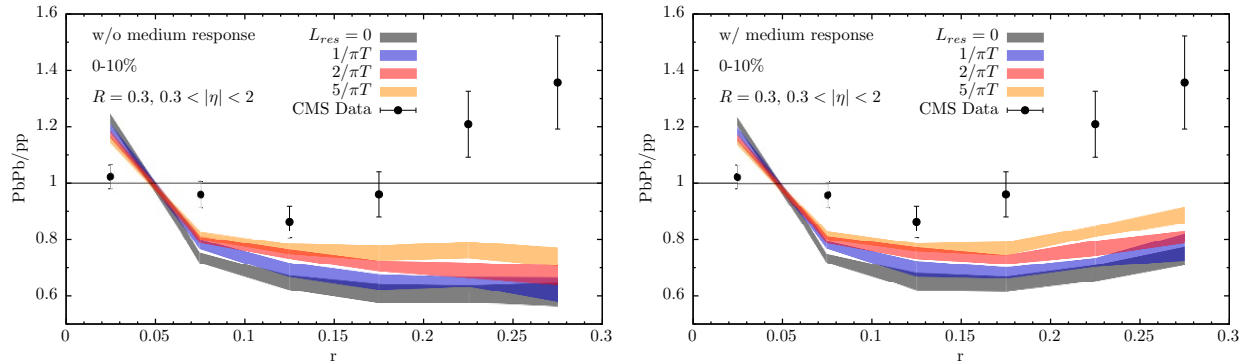
Figure 2.19: The hybrid model without (left) and with (right) the  $L_{\text{res}}$  parameter, compared to the jet  $R_{AA}$  as a function of jet  $p_T$  in two centrality intervals as measured in Ref. [119]. The different colors correspond to different jet radii. The Hybrid Model is fit to the 100–110 GeV point from the data, giving rise to the colored bands. Figure taken from [122].

468 Fixing the  $\kappa_{\text{sc}}$  parameter allows for predictions of other jet measurements like jet fragmentation and  
 469 jet shape. Figures 2.20(a) and 2.20(b) show a comparison of the measured and modeled values of the  
 470 modifications to the jet fragmentation and jet shape respectively. The model has also been compared to  
 471 measurements done by ATLAS, ALICE, and STAR [104, 120, 131] []

472 Here it can be seen that adding a medium response and a non-zero  $L_{\text{res}}$  parameter affects the prediction.  
 473 While the hard fragments (see Figure ??) are unaffected by the medium response, including the soft particles  
 474 from the wake compensates some of the suppression of soft fragments in Pb+Pb compared to  $pp$  collisions.  
 475 Moreover, including the  $L_{\text{res}}$  parameter further compensates the suppression for soft fragments, while reducing  
 476 the enhancement of the hard fragments. This is a result of allowing more hadrons carrying a smaller fraction  
 477 of the jet energy (low  $z$ , high  $(\ln(1/z))$ ) to survive into the final state. The jet shape observable (see Figure ??)



(a) The modification to the jet fragmentation from  $pp$  to  $Pb+Pb$  as a function of  $\ln(1/z)$  as measured in Ref. [132] compared to the predictions of the hybrid model. The predictions are shown without (left) and with (right) the effect of the wake from the QGP responding to the jet. The different colors correspond to different  $L_{res}$  parameters. Figure taken from [122].



(b) The modification to the jet shape from  $pp$  to  $Pb+Pb$  as a function of  $r$  as measured in Ref. [121] compared to the predictions of the hybrid model. The predictions are shown without (left) and with (right) the effect of the wake from the QGP responding to the jet. The different colors correspond to different  $L_{res}$  parameters. Figure taken from [122].

Figure 2.20: A comparison of measured data, MC, and the analytic calculation of the EQ model. Figure taken from [108]

478 quantifies the radial distribution of energy in terms of annuli around the jet axis. It can be seen that  
479 introducing the  $L_{\text{res}}$  parameter enhances the probability to find final state hadrons at larger distances from  
480 the jet axis. The jet core ( $r < 0.05$ ) is also affected, with the depletion only slowly evolving with an increasing  
481  $L_{\text{res}}$ . One must be careful before making conclusions though, since these modifications are made between jets  
482 that are quenched (in Pb+Pb ) and unquenched (in  $pp$  ). Taking into account the fact that wider jets lose  
483 more energy and that the jet spectrum rapidly falls off, there is a bias for finding narrower quenched jets  
484 than unquenched jets. This makes the jet shape after quenching narrower in Pb+Pb compared to  $pp$ . While  
485 the model is not fully able to capture the features in the data, including the medium response moves it in  
486 the correct direction. It can be suggested that the model is missing a description of the medium induced  
487 modification to the hadronization process or that the wakes in the plasma are not equilibrating.

# Bibliography

- 488 [1] G. Roland, K. Safarik and P. Steinberg, *Heavy-ion collisions at the LHC*, Prog. Part. Nucl. Phys. **77**  
489 (2014) 70 (cit. on p. 1).
- 490 [2] M. K. Gaillard, P. D. Grannis and F. J. Sciulli, *The Standard model of particle physics*, Rev. Mod.  
491 Phys. **71** (1999) S96, arXiv: [hep-ph/9812285 \[hep-ph\]](#) (cit. on p. 1).
- 492 [3] Wikimedia Commons, *Standard Model of Elementary Particles*, (2006), URL: [https://en.wikipedia.org/wiki/Standard\\_Model](https://en.wikipedia.org/wiki/Standard_Model) (cit. on p. 1).
- 494 [4] J Beringer et al., *Review of Particle Physics, 2012-2013. Review of Particle Properties*, Phys. Rev. D  
495 **86** (2012) 010001 (cit. on pp. 2, 3).
- 496 [5] D. J. Gross and F. Wilczek, *Ultraviolet Behavior of Non-Abelian Gauge Theories*, Phys. Rev. Lett. **30**  
497 (26 1973) 1343, URL: <https://link.aps.org/doi/10.1103/PhysRevLett.30.1343> (cit. on p. 4).
- 498 [6] D. J. Gross and F. Wilczek, *Asymptotically Free Gauge Theories. I*, Phys. Rev. D **8** (10 1973) 3633,  
499 URL: <https://link.aps.org/doi/10.1103/PhysRevD.8.3633> (cit. on p. 4).
- 500 [7] A. Deur et al., *High precision determination of the  $Q^2$  evolution of the Bjorken Sum*, Phys. Rev. D**90**  
501 (2014) 012009, arXiv: [1405.7854 \[nucl-ex\]](#) (cit. on p. 4).
- 502 [8] J. H. Kim et al., *A Measurement of  $\alpha_s(Q^2)$  from the Gross-Llewellyn Smith sum rule*, Phys. Rev. Lett.  
503 **81** (1998) 3595, arXiv: [hep-ex/9808015 \[hep-ex\]](#) (cit. on p. 4).
- 504 [9] G. Altarelli et al., *Determination of the Bjorken sum and strong coupling from polarized structure  
505 functions*, Nucl. Phys. **B496** (1997) 337, arXiv: [hep-ph/9701289 \[hep-ph\]](#) (cit. on p. 4).
- 506 [10] H. W. Kendall, *Deep inelastic scattering: Experiments on the proton and the observation of scaling*,  
507 Rev. Mod. Phys. **63** (3 1991) 597 (cit. on p. 4).
- 508 [11] A. L. Kataev, G. Parente and A. V. Sidorov, *Improved fits to the  $xF_3$  CCFR data at the next-to-next-to-  
509 leading order and beyond*, Phys. Part. Nucl. **34** (2003) 20, [Erratum: Phys. Part. Nucl.38,no.6,827(2007)],  
510 arXiv: [hep-ph/0106221 \[hep-ph\]](#) (cit. on p. 4).

- 511 [12] S. Alekhin, J. Blumlein and S. Moch, *Parton Distribution Functions and Benchmark Cross Sections*  
 512 *at NNLO*, Phys. Rev. **D86** (2012) 054009, arXiv: [1202.2281 \[hep-ph\]](#) (cit. on p. 4).
- 513 [13] S. Alekhin, J. Blumlein and S.-O. Moch, *ABM news and benchmarks*, PoS **DIS2013** (2013) 039, arXiv:  
 514 [1308.5166 \[hep-ph\]](#) (cit. on p. 4).
- 515 [14] J. Blumlein, H. Bottcher and A. Guffanti, *Non-singlet QCD analysis of deep inelastic world data at*  
 516  $O(\alpha_s^3)$ , Nucl. Phys. **B774** (2007) 182, arXiv: [hep-ph/0607200 \[hep-ph\]](#) (cit. on p. 4).
- 517 [15] H1 Collaboration, *Three- and Four-jet Production at Low  $x$  at HERA*, Eur. Phys. J. **C54** (2008) 389,  
 518 arXiv: [0711.2606 \[hep-ex\]](#) (cit. on p. 4).
- 519 [16] ZEUS Collaboration, *Forward-jet production in deep inelastic ep scattering at HERA*, Eur. Phys. J.  
 520 **C52** (2007) 515, arXiv: [0707.3093 \[hep-ex\]](#) (cit. on p. 4).
- 521 [17] ZEUS Collaboration, *Multi-jet cross-sections in charged current  $e^\pm p$  scattering at HERA*, Phys. Rev.  
 522 **D78** (2008) 032004, arXiv: [0802.3955 \[hep-ex\]](#) (cit. on p. 4).
- 523 [18] ZEUS Collaboration, *Inclusive dijet cross sections in neutral current deep inelastic scattering at HERA*,  
 524 Eur. Phys. J. **C70** (2010) 965, arXiv: [1010.6167 \[hep-ex\]](#) (cit. on p. 4).
- 525 [19] ZEUS Collaboration, *Inclusive-jet cross sections in NC DIS at HERA and a comparison of the  $kT$ ,*  
 526 *anti- $kT$  and SIScone jet algorithms*, Phys. Lett. **B691** (2010) 127, arXiv: [1003.2923 \[hep-ex\]](#) (cit. on  
 527 p. 4).
- 528 [20] H1 Collaboration, *Jet Production in ep Collisions at High  $Q^2$  and Determination of  $\alpha_s$* , Eur. Phys. J.  
 529 **C65** (2010) 363, arXiv: [0904.3870 \[hep-ex\]](#) (cit. on p. 4).
- 530 [21] E. D. Bloom et al., *High-Energy Inelastic  $e - p$  Scattering at  $6^\circ$  and  $10^\circ$* , Phys. Rev. Lett. **23** (16  
 531 1969) 930, URL: <https://link.aps.org/doi/10.1103/PhysRevLett.23.930> (cit. on p. 4).
- 532 [22] M. Breidenbach et al., *Observed Behavior of Highly Inelastic Electron-Proton Scattering*, Phys. Rev.  
 533 Lett. **23** (16 1969) 935, URL: <https://link.aps.org/doi/10.1103/PhysRevLett.23.935> (cit. on  
 534 p. 4).
- 535 [23] J. D. Bjorken, *Asymptotic Sum Rules at Infinite Momentum*, Phys. Rev. **179** (5 1969) 1547, URL:  
 536 <https://link.aps.org/doi/10.1103/PhysRev.179.1547> (cit. on p. 4).
- 537 [24] K. Nishijima, *BRS invariance, asymptotic freedom and color confinement (a review)*, Czechoslovak  
 538 Journal of Physics **46** (1996) 1, ISSN: 1572-9486, URL: <https://doi.org/10.1007/BF01692238>  
 539 (cit. on p. 4).

- 540 [25] K. G. Wilson, *Confinement of quarks*, Phys. Rev. D **10** (8 1974) 2445, URL: <https://link.aps.org/doi/10.1103/PhysRevD.10.2445> (cit. on p. 4).
- 541
- 542 [26] W. Buchmuller, *Fine- and hyperfine structure of quarkonia*, Physics Letters B **112** (1982) 479 ,  
543 ISSN: 0370-2693, URL: <http://www.sciencedirect.com/science/article/pii/0370269382908541>  
544 (cit. on p. 4).
- 545 [27] J. Kogut, D. Sinclair and L. Susskind, *A quantitative approach to low-energy quantum chromodynamics*,  
546 Nuclear Physics B **114** (1976) 199 , ISSN: 0550-3213, URL: <http://www.sciencedirect.com/science/article/pii/0550321376905861> (cit. on p. 4).
- 547
- 548 [28] N. Isgur and J. Paton, *Flux-tube model for hadrons in QCD*, Phys. Rev. D **31** (11 1985) 2910, URL:  
549 <https://link.aps.org/doi/10.1103/PhysRevD.31.2910> (cit. on p. 4).
- 550 [29] M. Faber, J. Greensite and OlejnkaS, *Casimir scaling from center vortices: Towards an understanding  
551 of the adjoint string tension*, Phys. Rev. D **57** (4 1998) 2603, URL: <https://link.aps.org/doi/10.1103/PhysRevD.57.2603> (cit. on p. 4).
- 552
- 553 [30] G. S. Bali, *Casimir scaling of SU(3) static potentials*, Phys. Rev. D **62** (11 2000) 114503, URL:  
554 <https://link.aps.org/doi/10.1103/PhysRevD.62.114503> (cit. on p. 4).
- 555 [31] J. B. Kogut, *The lattice gauge theory approach to quantum chromodynamics*, Rev. Mod. Phys. **55** (3  
556 1983) 775, URL: <https://link.aps.org/doi/10.1103/RevModPhys.55.775> (cit. on p. 4).
- 557 [32] D. Zwanziger, *No Confinement without Coulomb Confinement*, Phys. Rev. Lett. **90** (10 2003) 102001,  
558 URL: <https://link.aps.org/doi/10.1103/PhysRevLett.90.102001> (cit. on p. 4).
- 559 [33] A. Jaffe and E. Witten, *Yang-Mills and Mass Gap*, <http://www.claymath.org/millennium-problems/yang-mills-and-mass-gap> (cit. on p. 4).
- 560
- 561 [34] E. V. Shuryak, *Quantum chromodynamics and the theory of superdense matter*, Physics Reports **61**  
562 (1980) 71 , ISSN: 0370-1573 (cit. on pp. 4, 7).
- 563 [35] J. C. Collins and M. J. Perry, *Superdense Matter: Neutrons or Asymptotically Free Quarks?*, Phys.  
564 Rev. Lett. **34** (21 1975) 1353 (cit. on pp. 4, 6).
- 565 [36] A. D. Linde, *Phase transitions in gauge theories and cosmology*, Reports on Progress in Physics **42**  
566 (1979) 389 (cit. on p. 4).
- 567 [37] LIGO/VIRGO Collaboration, *GW170817: Observation of Gravitational Waves from a Binary Neutron  
568 Star Inspiral*, Phys. Rev. Lett. **119** (16 2017) 161101, URL: <https://link.aps.org/doi/10.1103/PhysRevLett.119.161101> (cit. on p. 4).
- 569

- 570 [38] S. Han and A. W. Steiner, *Tidal deformability with sharp phase transitions in (binary) neutron stars*,  
 571 Phys. Rev. **D99** (2019) 083014, arXiv: [1810.10967 \[nucl-th\]](https://arxiv.org/abs/1810.10967) (cit. on p. 4).
- 572 [39] J.-E. Christian, A. Zacchi and J. Schaffner-Bielich, *Signals in the tidal deformability for phase*  
 573 *transitions in compact stars with constraints from GW170817*, Phys. Rev. D **99** (2 2019) 023009, URL:  
 574 <https://link.aps.org/doi/10.1103/PhysRevD.99.023009> (cit. on p. 4).
- 575 [40] E. R. Most et al., *Signatures of Quark-Hadron Phase Transitions in General-Relativistic Neutron-Star*  
 576 *Mergers*, Phys. Rev. Lett. **122** (6 2019) 061101, URL: <https://link.aps.org/doi/10.1103/PhysRevLett.122.061101> (cit. on p. 4).
- 577 [41] A. Bauswein, H.-T. Janka, K. Hebeler and A. Schwenk, *Equation-of-state dependence of the gravitational-*  
 578 *wave signal from the ring-down phase of neutron-star mergers*, Phys. Rev. D **86** (6 2012) 063001, URL:  
 579 <https://link.aps.org/doi/10.1103/PhysRevD.86.063001> (cit. on p. 5).
- 580 [42] A. Bauswein et al., *Identifying a First-Order Phase Transition in Neutron-Star Mergers through*  
 581 *Gravitational Waves*, Phys. Rev. Lett. **122** (6 2019) 061102, URL: <https://link.aps.org/doi/10.1103/PhysRevLett.122.061102> (cit. on p. 5).
- 582 [43] S. Borsanyi et al., *Is there still any  $T_c$  mystery in lattice QCD? Results with physical masses in the*  
 583 *continuum limit III*, JHEP **09** (2010) 073, arXiv: [1005.3508 \[hep-lat\]](https://arxiv.org/abs/1005.3508) (cit. on p. 5).
- 584 [44] A. S. Kronfeld, *Twenty-first Century Lattice Gauge Theory: Results from the QCD Lagrangian*, Ann.  
 585 Rev. Nucl. Part. Sci. **62** (2012) 265, arXiv: [1203.1204 \[hep-lat\]](https://arxiv.org/abs/1203.1204) (cit. on p. 5).
- 586 [45] J. W. Harris and B. Muller, *The search for the quark-gluon plasma*, Annual Review of Nuclear and  
 587 Particle Science **46** (1996) 71, eprint: <https://doi.org/10.1146/annurev.nucl.46.1.71>, URL:  
 588 <https://doi.org/10.1146/annurev.nucl.46.1.71> (cit. on p. 5).
- 589 [46] PHENIX Collaboration, *Enhanced Production of Direct Photons in Au + Au Collisions at  $\sqrt{s_{NN}} =$*   
 590 *200 GeV and Implications for the Initial Temperature*, Phys. Rev. Lett. **104** (13 2010) 132301 (cit. on  
 591 p. 5).
- 592 [47] ALICE Collaboration, *Direct photon production in Pb–Pb collisions at  $s_{NN}=2.76$  TeV*, Physics Letters  
 593 **B 754** (2016) 235 , ISSN: 0370-2693 (cit. on p. 5).
- 594 [48] Z. Fodor and S. Katz, *Critical point of QCD at finite T and  $\mu$ , lattice results for physical quark masses*,  
 595 Journal of High Energy Physics **2004** (2004) 050 (cit. on p. 5).
- 596 [49] STAR Collaboration, *Experimental and theoretical challenges in the search for the quark-gluon plasma: The STAR Collaboration's critical assessment of the evidence from RHIC collisions*, Nuclear Physics  
 597 **A 757** (2005) 102 , First Three Years of Operation of RHIC, ISSN: 0375-9474 (cit. on p. 5).

- [50] ALICE Collaboration, *Production of light nuclei and anti-nuclei in pp and Pb-Pb collisions at energies available at the CERN Large Hadron Collider*, *Phys. Rev. C* **93** (2 2016) 024917 (cit. on p. 5).
- [51] PHENIX Collaboration, *Single identified hadron spectra from  $\sqrt{s_{NN}} = 130$  GeV Au + Au collisions*, *Phys. Rev. C* **69** (2 2004) 024904 (cit. on p. 5).
- [52] BRAHMS Collaboration, *Centrality dependent particle production at  $y = 0$  and  $y \geq 1$  in Au+Au collisions at  $\sqrt{s_{NN}} = 200$  GeV*, *Phys. Rev. C* **72** (1 2005) 014908 (cit. on p. 5).
- [53] PHOBOS Collaboration, *Identified hadron transverse momentum spectra in Au+Au collisions at  $\sqrt{s_{NN}} = 62.4$  GeV*, *Phys. Rev. C* **75** (2 2007) 024910 (cit. on p. 5).
- [54] ALICE Collaboration, *Centrality dependence of  $\pi$ ,  $K$ , and  $p$  production in Pb-Pb collisions at  $\sqrt{s_{NN}} = 2.76$  TeV*, *Phys. Rev. C* **88** (4 2013) 044910 (cit. on p. 5).
- [55] A. Ster, T. Csorgo and B. Lorstad, *The Reconstructed final state of Pb + Pb 158-GeV/A reactions from spectra and correlation data of NA49, NA44 and WA98*, *Nucl. Phys.* **A661** (1999) 419, arXiv: [hep-ph/9907338 \[hep-ph\]](#) (cit. on p. 6).
- [56] A. M. Poskanzer et al., *Centrality dependence of directed and elliptic flow at the SPS*, *Nucl. Phys.* **A661** (1999) 341, arXiv: [nucl-ex/9906013 \[nucl-ex\]](#) (cit. on p. 6).
- [57] C. Pinkenburg et al., *Elliptic flow: Transition from out-of-plane to in-plane emission in Au + Au collisions*, *Phys. Rev. Lett.* **83** (1999) 1295, arXiv: [nucl-ex/9903010 \[nucl-ex\]](#) (cit. on p. 6).
- [58] ATLAS Collaboration, *Measurement of the azimuthal anisotropy of charged particles produced in  $\sqrt{s_{NN}} = 5.02$  TeV Pb+Pb collisions with the ATLAS detector*, *Eur. Phys. J. C* **78** (2018) 997, arXiv: [1808.03951 \[nucl-ex\]](#) (cit. on p. 6).
- [59] PHENIX Collaboration, *Elliptic Flow of Identified Hadrons in Au + Au Collisions at  $\sqrt{s_{NN}} = 200$  GeV*, *Phys. Rev. Lett.* **91** (18 2003) 182301 (cit. on p. 6).
- [60] CMS Collaboration, *Non-Gaussian elliptic-flow fluctuations in PbPb collisions at  $\sqrt{s_{NN}} = 5.02$  TeV*, *Phys. Lett. B* **789** (2019) 643, arXiv: [1711.05594 \[nucl-ex\]](#) (cit. on p. 6).
- [61] ALICE Collaboration, *Anisotropic Flow of Charged Particles in Pb-Pb Collisions at  $\sqrt{s_{NN}} = 5.02$  TeV*, *Phys. Rev. Lett.* **116** (13 2016) 132302 (cit. on p. 6).
- [62] M. Connors, C. Nattrass, R. Reed and S. Salur, *Jet measurements in heavy ion physics*, *Rev. Mod. Phys.* **90** (2 2018) 025005 (cit. on p. 6).
- [63] A. M. Poskanzer and S. A. Voloshin, *Methods for analyzing anisotropic flow in relativistic nuclear collisions*, *Phys. Rev. C* **58** (1998) 1671, arXiv: [nucl-ex/9805001 \[nucl-ex\]](#) (cit. on p. 6).

- [631] [64] U. Heinz and R. Snellings, *Collective flow and viscosity in relativistic heavy-ion collisions*, *Ann. Rev. Nucl. Part. Sci.* **63** (2013) 123, arXiv: [1301.2826 \[nucl-th\]](#) (cit. on p. 6).
- [632] [633] [65] H. Niemi, K. J. Eskola and R. Paatelainen, *Event-by-event fluctuations in a perturbative QCD + saturation + hydrodynamics model: Determining QCD matter shear viscosity in ultrarelativistic heavy-ion collisions*, *Phys. Rev. C* **93** (2016) 024907, arXiv: [1505.02677 \[hep-ph\]](#) (cit. on p. 7).
- [634] [635] [636] [66] ALICE Collaboration, *Higher harmonic anisotropic flow measurements of charged particles in Pb-Pb collisions at  $\sqrt{s_{NN}}=2.76$  TeV*, *Phys. Rev. Lett.* **107** (2011) 032301, arXiv: [1105.3865 \[nucl-ex\]](#) (cit. on p. 7).
- [637] [638] [639] [67] J. D. Bjorken, *Highly relativistic nucleus-nucleus collisions: The central rapidity region*, *Phys. Rev. D* **27** (1 1983) 140 (cit. on p. 6).
- [640] [641] [68] PHENIX Collaboration, *Formation of dense partonic matter in relativistic nucleus-nucleus collisions at RHIC: Experimental evaluation by the PHENIX collaboration*, *Nucl. Phys. A* **757** (2005) 184, arXiv: [nucl-ex/0410003 \[nucl-ex\]](#) (cit. on p. 7).
- [642] [643] [644] [69] CMS Collaboration, *Charged hadron multiplicity and transverse energy densities in PbPb collisions from CMS*, *Journal of Physics G: Nuclear and Particle Physics* **38** (2011) 124041 (cit. on p. 7).
- [645] [646] [70] B. Muller, J. Schukraft and B. Wyslouch, *First Results from Pb+Pb collisions at the LHC*, *Ann. Rev. Nucl. Part. Sci.* **62** (2012) 361, arXiv: [1202.3233 \[hep-ex\]](#) (cit. on p. 8).
- [647] [648] [71] W. Busza et al., *Heavy Ion Collisions: The Big Picture, and the Big Questions*, *Ann. Rev. Nucl. Part. Sci.* **68** (2018) 339, arXiv: [1802.04801 \[hep-ph\]](#) (cit. on pp. 6, 9).
- [649] [72] R. Glauber, *Lectures in theoretical physics*, ed. WE Brittin and LG Dunham, Interscience, New York **1** (1959) 315 (cit. on p. 8).
- [650] [73] R. Glauber et al., *Lectures in theoretical physics*, 1959 (cit. on p. 8).
- [651] [652] [74] H. D. Vries, C. D. Jager and C. D. Vries, *Nuclear charge-density-distribution parameters from elastic electron scattering*, *Atomic Data and Nuclear Data Tables* **36** (1987) 495 , ISSN: 0092-640X (cit. on pp. 9, 10).
- [653] [654] [75] M. L. Miller, K. Reygers, S. J. Sanders and P. Steinberg, *Glauber Modeling in High-Energy Nuclear Collisions*, *Annual Review of Nuclear and Particle Science* **57** (2007) 205 (cit. on pp. 9, 10, 12, 21).
- [655] [656] [76] B. Alver, M. Baker, C. Loizides and P. Steinberg, *The PHOBOS Glauber Monte Carlo*, (2008), arXiv: [0805.4411 \[nucl-ex\]](#) (cit. on p. 9).

- 660 [77] D. Kharzeev and M. Nardi, *Hadron production in nuclear collisions at RHIC and high density QCD*,  
 661 *Phys. Lett.* **B507** (2001) 121, arXiv: [nucl-th/0012025 \[nucl-th\]](#) (cit. on p. 11).
- 662 [78] A. Bialas, M. Bleszynski and W. Czyz, *Multiplicity Distributions in Nucleus-Nucleus Collisions at*  
 663 *High-Energies*, *Nucl. Phys.* **B111** (1976) 461 (cit. on p. 11).
- 664 [79] ATLAS Collaboration, *Centrality determination in  $\sqrt{s_{\text{NN}}} = 5.02 \text{ TeV} \text{ Pb+Pb}$  collision data in 2015*,  
 665 tech. rep. ATL-COM-PHYS-2016-1287, CERN, 2016 (cit. on p. 12).
- 666 [80] T. Sjostrand, S. Mrenna and P. Z. Skands, *A Brief Introduction to PYTHIA 8.1*, *Comput. Phys.*  
 667 *Commun.* **178** (2008) 852, arXiv: [0710.3820 \[hep-ph\]](#) [hep-ph] (cit. on p. 13).
- 668 [81] G.-Y. Qin and X.-N. Wang, *Jet quenching in high-energy heavy-ion collisions*, *Int. J. Mod. Phys. E*  
 669 **24** (2015) 1530014, [,309(2016)], arXiv: [1511.00790 \[hep-ph\]](#) [hep-ph] (cit. on pp. 13, 15).
- 670 [82] A. D. Martin, W. J. Stirling, R. S. Thorne and G. Watt, *Parton distributions for the LHC*, *The European*  
 671 *Physical Journal C* **63** (2009) 189, ISSN: 1434-6052, URL: <https://doi.org/10.1140/epjc/s10052-009-1072-5> (cit. on p. 14).
- 673 [83] M. Hirai, S. Kumano and T.-H. Nagai, *Determination of nuclear parton distribution functions and*  
 674 *their uncertainties at next-to-leading order*, *Phys. Rev. C* **76** (6 2007) 065207 (cit. on p. 14).
- 675 [84] D. de Florian and R. Sassot, *Nuclear parton distributions at next to leading order*, *Phys. Rev. D* **69** (7  
 676 2004) 074028 (cit. on p. 14).
- 677 [85] K. Eskola, H Paukkunen and C. Salgado, *EPS09 — A new generation of NLO and LO nuclear parton*  
 678 *distribution functions*, *Journal of High Energy Physics* **2009** (2009) 065 (cit. on p. 14).
- 679 [86] S. J. Brodsky and H. J. Lu, *Shadowing and antishadowing of nuclear structure functions*, *Phys. Rev.*  
 680 *Lett.* **64** (12 1990) 1342 (cit. on p. 14).
- 681 [87] European Muon Collaboration, *The ratio of the nucleon structure functions F2N for iron and deuterium*,  
 682 *Physics Letters B* **123** (1983) 275 , ISSN: 0370-2693 (cit. on p. 14).
- 683 [88] O. Hen, E. Piasetzky and L. B. Weinstein, *New data strengthen the connection between short range*  
 684 *correlations and the EMC effect*, *Phys. Rev. C* **85** (4 2012) 047301 (cit. on p. 14).
- 685 [89] K. Saito and T. Uchiyama, *Effect of the Fermi Motion on Nuclear Structure Functions and the Emc*  
 686 *Effect*, *Z. Phys. A* **322** (1985) 299 (cit. on p. 15).
- 687 [90] CMS Collaboration, *Jet momentum dependence of jet quenching in PbPb collisions at sNN=2.76 TeV*,  
 688 *Physics Letters B* **712** (2012) 176 , ISSN: 0370-2693 (cit. on p. 15).

- 689 [91] ATLAS collaboration, *Study of inclusive jet yields in Pb+Pb collisions at  $\sqrt{s_{NN}} = 5.02$  TeV*, (2017)  
 690 (cit. on p. 15).
- 691 [92] The CMS collaboration, *Measurement of transverse momentum relative to dijet systems in PbPb and*  
 692 *pp collisions at  $\sqrt{s_{NN}} = 2.76$  TeV*, *Journal of High Energy Physics* **2016** (2016) 6, ISSN: 1029-8479,  
 693 URL: [https://doi.org/10.1007/JHEP01\(2016\)006](https://doi.org/10.1007/JHEP01(2016)006) (cit. on p. 15).
- 694 [93] S. Chatrchyan et al., *Jet momentum dependence of jet quenching in PbPb collisions at  $\sqrt{s_{NN}} = 2.76$*   
 695 *TeV*, *Phys. Lett. B* **712** (2012) 176, arXiv: [1202.5022 \[nucl-ex\]](https://arxiv.org/abs/1202.5022) (cit. on p. 15).
- 696 [94] R. Baier, Y. Dokshitzer, A. Mueller, S. Peigné and D. Schiff, *Radiative energy loss of high energy*  
 697 *quarks and gluons in a finite-volume quark-gluon plasma*, *Nuclear Physics B* **483** (1997) 291 , ISSN:  
 698 0550-3213 (cit. on p. 15).
- 699 [95] M. Gyulassy, P. Levai and I. Vitev, *Jet quenching in thin quark gluon plasmas. 1. Formalism*, *Nucl.*  
 700 *Phys. B* **571** (2000) 197, arXiv: [hep-ph/9907461 \[hep-ph\]](https://arxiv.org/abs/hep-ph/9907461) (cit. on p. 15).
- 701 [96] U. A. Wiedemann, *Gluon radiation off hard quarks in a nuclear environment: Opacity expansion*, *Nucl.*  
 702 *Phys. B* **588** (2000) 303, arXiv: [hep-ph/0005129 \[hep-ph\]](https://arxiv.org/abs/hep-ph/0005129) (cit. on p. 15).
- 703 [97] P. B. Arnold, G. D. Moore and L. G. Yaffe, *Photon emission from ultrarelativistic plasmas*, *JHEP* **11**  
 704 (2001) 057, arXiv: [hep-ph/0109064 \[hep-ph\]](https://arxiv.org/abs/hep-ph/0109064) (cit. on p. 15).
- 705 [98] X.-F. Guo and X.-N. Wang, *Multiple scattering, parton energy loss and modified fragmentation*  
 706 *functions in deeply inelastic e A scattering*, *Phys. Rev. Lett.* **85** (2000) 3591, arXiv: [hep-ph/0005044](https://arxiv.org/abs/hep-ph/0005044)  
 707 [\[hep-ph\]](https://arxiv.org/abs/hep-ph/0005044) (cit. on p. 15).
- 708 [99] M. Cacciari, G. P. Salam and G. Soyez, *The Anti- $k(t)$  jet clustering algorithm*, *JHEP* **0804** (2008) 063,  
 709 arXiv: [0802.1189 \[hep-ph\]](https://arxiv.org/abs/0802.1189) (cit. on pp. 16, 17).
- 710 [100] S. Catani, Y. L. Dokshitzer, M. H. Seymour and B. R. Webber, *Longitudinally invariant  $K_t$  clustering*  
 711 *algorithms for hadron hadron collisions*, *Nucl. Phys. B* **406** (1993) 187 (cit. on p. 17).
- 712 [101] Y. L. Dokshitzer, G. D. Leder, S. Moretti and B. R. Webber, *Better jet clustering algorithms*, *JHEP*  
 713 **08** (1997) 001, arXiv: [hep-ph/9707323 \[hep-ph\]](https://arxiv.org/abs/hep-ph/9707323) (cit. on p. 17).
- 714 [102] G. P. Salam, *Towards Jetography*, *Eur. Phys. J. C* **67** (2010) 637, arXiv: [0906.1833 \[hep-ph\]](https://arxiv.org/abs/0906.1833) (cit. on  
 715 p. 17).
- 716 [103] G. P. Salam and G. Soyez, *A practical seedless infrared-safe cone jet algorithm*, *Journal of High Energy*  
 717 *Physics* **2007** (2007) 086 (cit. on p. 18).

- 718 [104] ATLAS Collaboration, *Measurement of the jet radius and transverse momentum dependence of*  
 719 *inclusive jet suppression in lead-lead collisions at  $\sqrt{s_{NN}} = 2.76 \text{ TeV}$  with the ATLAS detector*, *Phys.*  
 720 *Lett.* **B719** (2013) 220, arXiv: [1208.1967 \[hep-ex\]](#) (cit. on pp. 18, 37).
- 721 [105] ATLAS Collaboration, *Measurement of jet  $p_T$  correlations in Pb+Pb and pp collisions at  $\sqrt{s_{NN}} = 2.76$*   
 722 *TeV with the ATLAS detector*, *Phys. Lett.* **B774** (2017) 379, arXiv: [1706.09363 \[hep-ex\]](#) (cit. on  
 723 pp. 19–21).
- 724 [106] ATLAS Collaboration, *Measurement of the nuclear modification factor for inclusive jets in Pb+Pb*  
 725 *collisions at  $\sqrt{s_{NN}} = 5.02 \text{ TeV}$  with the ATLAS detector*, *Phys. Lett.* **B790** (2019) 108, arXiv:  
 726 [1805.05635 \[nucl-ex\]](#) (cit. on pp. 20, 22, 23).
- 727 [107] ATLAS Collaboration, *Measurement of jet fragmentation in Pb+Pb and pp collisions at  $\sqrt{s_{NN}} = 5.02$*   
 728 *TeV with the ATLAS detector*, *Phys. Rev.* **C98** (2018) 024908, arXiv: [1805.05424 \[nucl-ex\]](#) (cit. on  
 729 pp. 23–26).
- 730 [108] M. Spousta and B. Cole, *Interpreting single jet measurements in Pb + Pb collisions at the LHC*, *Eur.*  
 731 *Phys. J. C* **76** (2016) 50, arXiv: [1504.05169 \[hep-ph\]](#) (cit. on pp. 24, 26, 28–30, 38).
- 732 [109] Y.-T. Chien et al., *Jet Quenching from QCD Evolution*, *Phys. Rev.* **D93** (2016) 074030, arXiv:  
 733 [1509.02936 \[hep-ph\]](#) (cit. on p. 24).
- 734 [110] Z.-B. Kang et al., *Inclusive production of small radius jets in heavy-ion collisions*, *Phys. Lett.* **B769**  
 735 (2017) 242, arXiv: [1701.05839 \[hep-ph\]](#) (cit. on p. 24).
- 736 [111] J. Casalderrey-Solana et al., *A Hybrid Strong/Weak Coupling Approach to Jet Quenching*, *JHEP* **10**  
 737 (2014) 019, arXiv: [1405.3864 \[hep-ph\]](#) (cit. on pp. 26, 34).
- 738 [112] CMS Collaboration, *Observation and studies of jet quenching in PbPb collisions at nucleon-nucleon*  
 739 *center-of-mass energy = 2.76 TeV*, *Phys. Rev.* **C84** (2011) 024906, arXiv: [1102.1957 \[nucl-ex\]](#)  
 740 (cit. on p. 27).
- 741 [113] J.-P. Blaizot, E. Iancu and Y. Mehtar-Tani, *Medium-induced QCD cascade: democratic branching and*  
 742 *wave turbulence*, *Phys. Rev. Lett.* **111** (2013) 052001, arXiv: [1301.6102 \[hep-ph\]](#) (cit. on p. 27).
- 743 [114] J. Casalderrey-Solana, Y. Mehtar-Tani, C. A. Salgado and K. Tywoniuk, *New picture of jet quenching*  
 744 *dictated by color coherence*, *Phys. Lett.* **B725** (2013) 357, arXiv: [1210.7765 \[hep-ph\]](#) (cit. on p. 27).
- 745 [115] R. Baier, Y. L. Dokshitzer, A. H. Mueller and D. Schiff, *Quenching of hadron spectra in media*, *JHEP*  
 746 **09** (2001) 033, arXiv: [hep-ph/0106347 \[hep-ph\]](#) (cit. on p. 28).

- 747 [116] ATLAS Collaboration, *Measurements of the Nuclear Modification Factor for Jets in Pb+Pb Collisions*  
 748 at  $\sqrt{s_{NN}} = 2.76$  TeV with the ATLAS Detector, *Phys. Rev. Lett.* **114** (2015) 072302, arXiv: [1411.2357](#)  
 749 [[hep-ex](#)] (cit. on pp. 30, 31).
- 750 [117] ATLAS Collaboration, *Measurement of inclusive jet charged-particle fragmentation functions in*  
 751 *Pb+Pb collisions at  $\sqrt{s_{NN}} = 2.76$  TeV with the ATLAS detector*, *Phys. Lett. B* **739** (2014) 320, arXiv:  
 752 [1406.2979](#) [[hep-ex](#)] [[hep-ex](#)] (cit. on p. 30).
- 753 [118] Y. Tachibana, N.-B. Chang and G.-Y. Qin, *Full jet in quark-gluon plasma with hydrodynamic medium*  
 754 *response*, *Phys. Rev. C* **95** (2017) 044909, arXiv: [1701.07951](#) [[nucl-th](#)] (cit. on pp. 31–35).
- 755 [119] CMS Collaboration, *Measurement of inclusive jet cross sections in pp and PbPb collisions at  $\sqrt{s_{NN}} =$*   
 756 *2.76 TeV*, *Phys. Rev. C* **96** (2017) 015202, arXiv: [1609.05383](#) [[nucl-ex](#)] (cit. on pp. 31, 33, 34, 36,  
 757 37).
- 758 [120] ALICE Collaboration, *Measurement of charged jet suppression in Pb-Pb collisions at  $\sqrt{s_{NN}} = 2.76$*   
 759 *TeV*, *JHEP* **03** (2014) 013, arXiv: [1311.0633](#) [[nucl-ex](#)] (cit. on pp. 31, 37).
- 760 [121] CMS Collaboration, *Modification of jet shapes in PbPb collisions at  $\sqrt{s_{NN}} = 2.76$  TeV*, *Phys. Lett.*  
 761 *B730* (2014) 243, arXiv: [1310.0878](#) [[nucl-ex](#)] [[nucl-ex](#)] (cit. on pp. 35, 38).
- 762 [122] Z. Hulcher et al., *Resolution Effects in the Hybrid Strong/Weak Coupling Model*, (2017), arXiv:  
 763 [1707.05245](#) [[hep-ph](#)] (cit. on pp. 34, 36–38).
- 764 [123] J. Casalderrey-Solana et al., *Angular Structure of Jet Quenching Within a Hybrid Strong/Weak*  
 765 *Coupling Model*, *JHEP* **03** (2017) 135, arXiv: [1609.05842](#) [[hep-ph](#)] (cit. on pp. 34, 36).
- 766 [124] P. M. Chesler and K. Rajagopal, *On the Evolution of Jet Energy and Opening Angle in Strongly*  
 767 *Coupled Plasma*, *JHEP* **05** (2016) 098, arXiv: [1511.07567](#) [[hep-th](#)] (cit. on p. 35).
- 768 [125] P. M. Chesler and K. Rajagopal, *Jet quenching in strongly coupled plasma*, *Phys. Rev. D* **90** (2014) 025033,  
 769 arXiv: [1402.6756](#) [[hep-th](#)] (cit. on p. 35).
- 770 [126] P. Jacobs and X.-N. Wang, *Matter in extremis: Ultrarelativistic nuclear collisions at RHIC*, *Prog. Part.*  
 771 *Nucl. Phys.* **54** (2005) 443, arXiv: [hep-ph/0405125](#) [[hep-ph](#)] (cit. on p. 35).
- 772 [127] A. Majumder and M. Van Leeuwen, *The Theory and Phenomenology of Perturbative QCD Based Jet*  
 773 *Quenching*, *Prog. Part. Nucl. Phys.* **66** (2011) 41, arXiv: [1002.2206](#) [[hep-ph](#)] (cit. on p. 35).
- 774 [128] J. Casalderrey-Solana, H. Liu, D. Mateos, K. Rajagopal and U. A. Wiedemann, *Gauge/String Duality,*  
 775 *Hot QCD and Heavy Ion Collisions*, (2011), arXiv: [1101.0618](#) [[hep-th](#)] (cit. on p. 35).

- 776 [129] J. Casalderrey-Solana, J. G. Milhano and P. Quiroga-Arias, *Out of Medium Fragmentation from*  
777 *Long-Lived Jet Showers*, Phys. Lett. **B710** (2012) 175, arXiv: [1111.0310 \[hep-ph\]](#) (cit. on p. 35).
- 778 [130] T. Hirano, P. Huovinen and Y. Nara, *Elliptic flow in Pb+Pb collisions at  $\sqrt{s_{NN}} = 2.76 \text{ TeV}$ : hybrid*  
779 *model assessment of the first data*, Phys. Rev. **C84** (2011) 011901, arXiv: [1012.3955 \[nucl-th\]](#)  
780 (cit. on p. 36).
- 781 [131] J. Rusnak, *Inclusive spectrum of charged jets in central Au+Au collisions at  $\sqrt{s_{NN}} = 200 \text{ GeV}$  by*  
782 *STAR*, PoS **EPS-HEP2013** (2013) 191 (cit. on p. 37).
- 783 [132] CMS Collaboration, *Measurement of jet fragmentation in PbPb and pp collisions at  $\sqrt{s_{NN}} = 2.76$*   
784 *TeV*, Phys. Rev. **C 90** (2014) 024908, arXiv: [1406.0932\[nucl-ex\] \[nucl-ex\]](#) (cit. on p. 38).